Final Report

Project Title: Novel Fast Pyrolysis/Catalytic Technology for the Production of Stable Upgraded Liquids
Award Number: DE-FG36-08GO18214

Recipient: Virginia Tech
Project Location: Virginia Tech, Blacksburg, VA and University of Delaware, Newark, DE, Utah State University, Logan UT

Reporting Period: Sept. 30, 2008-March 31, 2012
Date of Report: April 20, 2012
Written by: Ted Oyama, Foster Agblevor, Francine Battaglia, Michael Klein
Program Manager: Angela Page
Principal Investigators: Ted Oyama, Foster Agblevor, Francine Battaglia, Michael Klein

Cost-Sharing Partners: BASF Chemicals, LLC
DOE Project Team:
Project Officer: Bryna Berendzen
Contracting Officer: Melissa Wise
Financial Assistance Officer: Geoffrey Walker
Project Monitor: Cynthia Tyler

Acknowledgment: This material is based upon work supported by the Department of Energy under Award Number DE-FG36-08GO18214

Novel Fast Pyrolysis/Catalytic Technology for the Production of Stable Upgraded Liquids

DE-FG36-08GO18214

Task number: A. Design, synthesis, and characterization of catalysts with multiple functions (Oyama)

1. **Planned Activities**:
   - A.1 Application of catalyst characterization methods
   - A.2 Cracking function development
   - A.3 HDO function development
   - A.4. Synthesis of new catalysts

2. **Actual Accomplishments**:

A principal goal of our project is the development of new catalysts for the upgrading of bio-oil. The most important function of the catalysts will be deoxygenation, so this was the first target of catalyst design. Conventional catalysts are sulfides like CoMo and NiMo supported on Al_2O_3, and these will be tried. A problem with sulfides is that they are known to deactivate when sulfur partial pressures are low and for this reason a number of other compositions are targeted. The compositions are principally transition metal phosphides, which are excellent hydrogenation catalysts. The latter are exemplified by MoP, WP, CoP, Fe_2P, Ni_2P, and mixed-metal phosphides. Considerable efforts will be made in relating the properties of the materials to their catalytic performance, and thus measurement of their physical characteristics is an integral part of the program. Comparison between catalysts will be fundamental, so the turnover frequency (TOF), the rate of reaction normalized to surface sites, will be determined. This will give a measure of the intrinsic activity, and will be useful for knowing whether improvements are necessary. For metallic catalysts, chemisorption of CO and H_2 will be used, and for sulfides low-temperature chemisorption of O_2 will be employed.

The preparation of the materials involves two steps, first the impregnation of precursor compounds (metal nitrates and ammonium phosphate) onto a silica support, and calcinations to form phosphate precursors, and second, the temperature-programmed reduction of the precursors to the phosphides. An example of a synthesis of Ni_2P/SiO_2 is given below (Fig. 1) using as support Cabosil EH5. The figure shows the mass spectrometer signal of water produced in the reduction of the phosphate. The peak temperature was 841 K (564 ^oC).

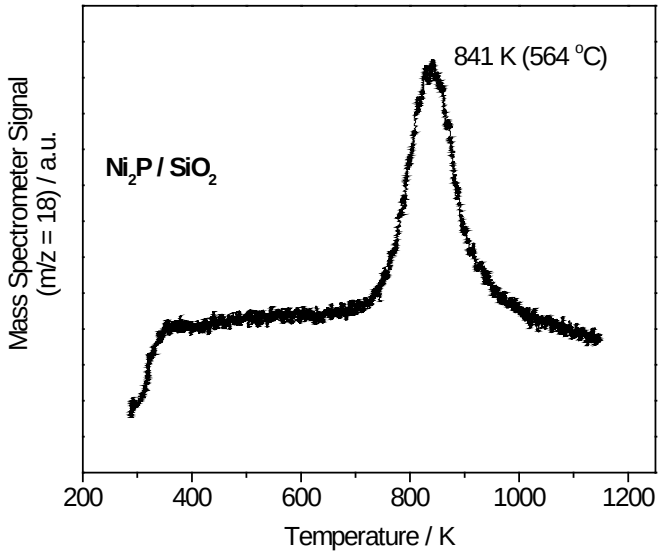

Figure 1. Temperature-programmed synthesis of Ni_2P/SiO_2

The sample was characterized by x-ray diffraction analysis (Fig. 2). A comparison to a powder diffraction file standard shows that the sample is Ni_2P. The broadening of the peaks is due to the small particle size, which can be estimated to be 5 nm from the Scherer equation.

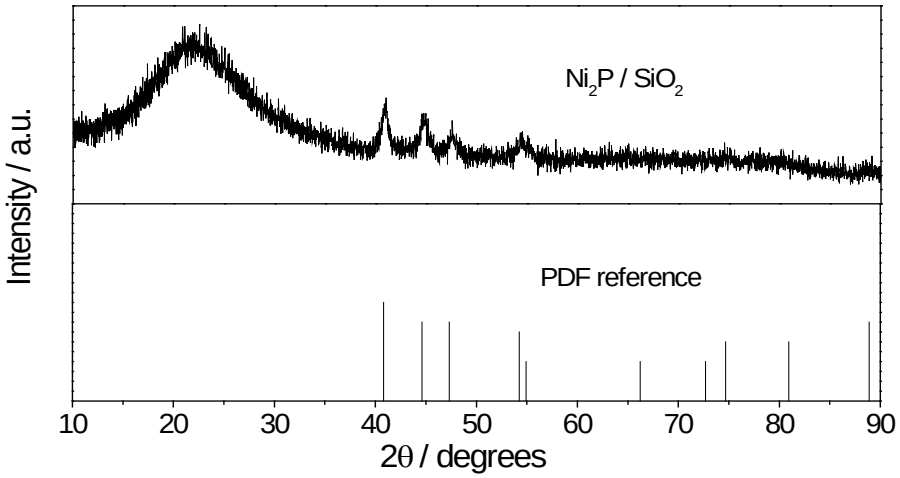

Figure 2. X-ray diffraction characterization of Ni_2P/SiO_2.

Other materials prepared were CoP, Fe_2P, and WP. Aside from x-ray diffraction analysis, the samples were characterized by BET surface area determinations and active site measurements. The active sites were measured by the chemisorptions of carbon monoxide. The results are summarized below.

	Co Uptake μmol/g	BET Surface Area m^2/g
WP/SiO_2 (EH5)	70	147
CoP/ SiO_2 (EH5)	42	307
Fe_2P/ SiO_2 (EH5)	52	233
Ni_2P/ SiO_2 (EH5)	134	309

The materials were tested for HDO of a model compound, guaiacol. Guaiacol is a pyrolytic decomposition product found in bio-oils and derives from guaiacylic lignin which is mostly found in softwoods but is also abundant in hardwoods. This is an excellent model compound representing the lignin decomposition products.

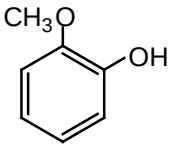

Guaiacol

The experimental unit for testing and the conditions are shown below.

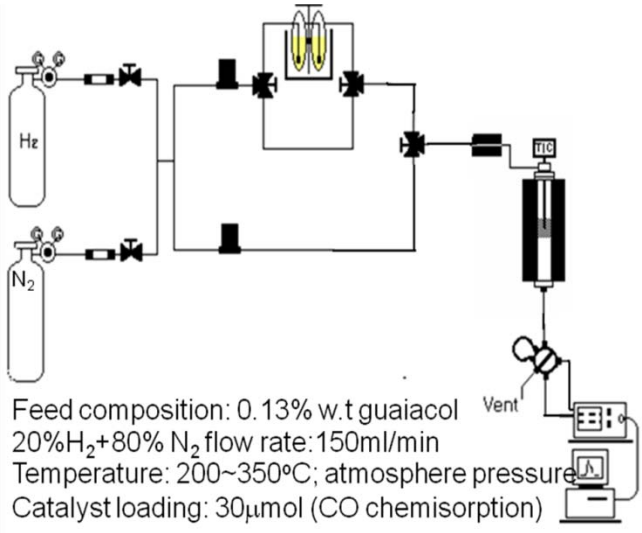

The unit was a packed-bed reactor and the analytical system was a gas chromatograph with a flame ionization detector. Products of reaction were identified with a gas-chromatograph-mass spectrometer. The principal products were phenol, methoxybenzene, and benzene.

Figure 3. Experimental unit for HDO testing

The turnover frequency based on active sites titrated by the chemisorption of CO followed the order: $Ni_2P > Co_2P > Fe_2P$, WP, MoP. The major products from hydrodeoxygenation of guaiacol for the most active phosphides were benzene and phenol, with a small amount of methoxybenzene formed. Kinetic studies revealed the formation of reaction intermediates such as catechol and cresol at short contact times. A commercial catalyst 5% Pd/Al_2O_3 was more active than the metal phosphides at lower contact time but produced only catechol. A commercial $CoMoS/Al_2O_3$ deactivated quickly and showed little activity for the HDO of guaiacol at these conditions. Thus, transition metal phosphides are promising materials for catalytic HDO of biofuels.

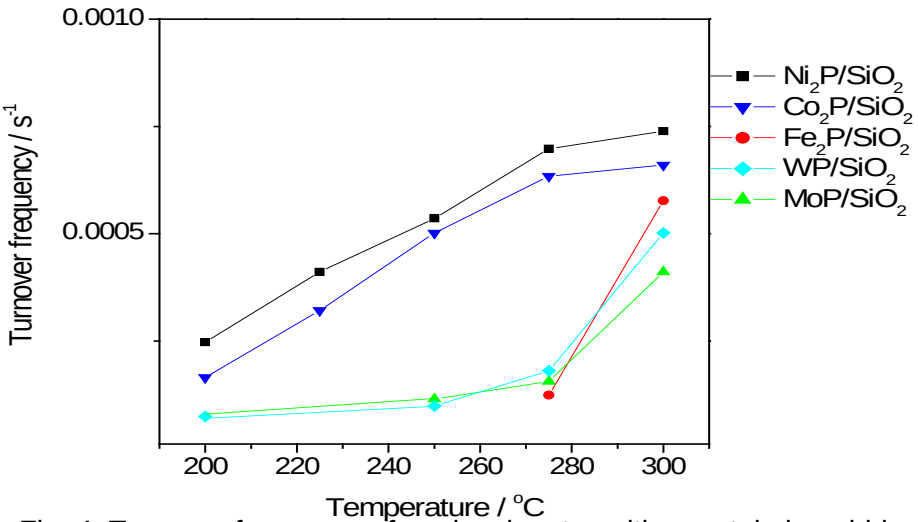

Fig. 4. Turnover frequency of guaiacol on transition metal phosphides

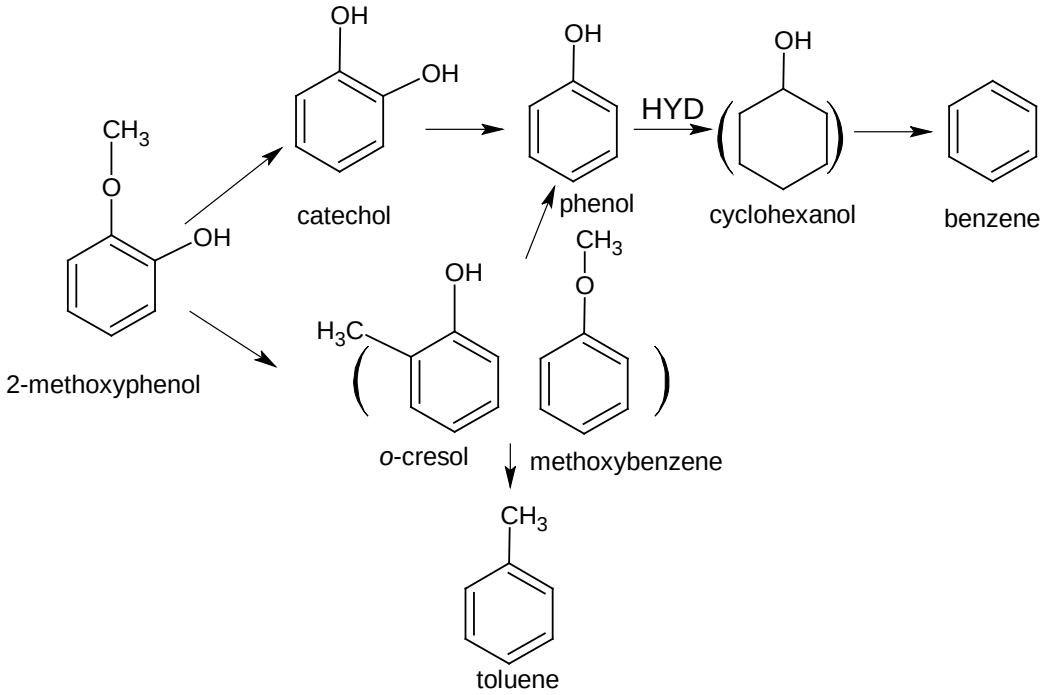

Fig. 5. Reaction network for HDO of guaiacol

Experimental Conditions:

Catalyst charge: 0.500 g Ni_2P/EH-5 Silica catalyst corresponding to a CO uptake of 80 µmol
Reactor pressure: 15 atm
Catalyst volume: 2 mL (includes volume of 0.500 g quartz chips to dilute the bed)
Composition of the mixed feed: 5 wt.% guaiacol, 1 wt.% n-decane (IS), 94 wt.% hexadecane
LHSV: 2.5 mL of mixed feed/mL cat. H Hydrogen flow: 150 mL (NTP)/min

Table 1 Reactivity Studies of Guaiacol HDO on Ni_2P/EH-5 Silica Catalyst

	300 °C (smp-1)	300 °C (smp-2)	300 °C (smp-3)	300 °C (smp-4)
Guaiacol conversion[1]	24.6	12.9	9.9	9.3
TOF (sec^{-1})[2]	0.00139	0.000727	0.000558	0.000525
Product distributions (%)				
Benzene	5.0	3.4	3.6	3.5
Toluene	8.7	4.2	3.4	3.5
Anisole	45.7	48.6	49.5	49.4
Phenol	40.6	43.8	43.5	43.5
m-cresol, o-cresol	ND[3]	ND	ND	ND
Pyrocatechol	ND	ND	ND	ND
Cyclohexane	NA[4]	NA	NA	NA

Notes: [1]Guaiacol conversion = $((C_{guaiacol,\ in} - C_{guaiacol,\ out})/(C_{guaiacol,\ in})) \times 100$

[2]TOF = $\frac{\text{Guaiacol flowrate (µmol per s) x conversion}}{\text{CO uptake (µmol per g) x catalyst weight (g)}}$ [3]ND = Not detected [4]NA = Not analyzed

Table 2. Reactivity Studies of Guaiacol HDO on Ni_2P/EH-5 Silica Catalyst as a function of Temperature (continued):

	285 °C (smp-1)	285 °C (smp-2)	270 °C (smp-1)	270 °C (smp-2)
Guaiacol conversion[1]	8.8	7.7	6.2	5.4
TOF (sec^{-1})[2]	0.000496	0.000434	0.000349	0.000304
Product distributions (%)				
Benzene	2.8	2.4	2.6	2.0
Toluene	2.9	3.1	2.3	1.7
Anisole	48.3	50.9	54.5	56.4
Phenol	45.9	43.6	40.8	39.9
m-cresol, o-cresol	ND[3]	ND	ND	ND
Pyrocatechol	ND	ND	ND	ND
Cyclohexane	NA[4]	NA	NA	NA

Table 3. Reactivity Studies of Guaiacol HDO on Ni2P/EH-5 Silica Catalyst as a function of Temperature (continued):

	255 °C (smp-1)	255 °C (smp-2)	300 °C (final-1)	300 °C (final-2)
Guaiacol conversion[1]	4.9	4.4	4.4	5.2
TOF (sec^{-1})[2]	0.000276	0.000248	0.000248	0.000293
Product distributions (%)				
Benzene	2.1	1.6	1.8	1.6
Toluene	0.0	0.0	0.0	0.0
Anisole	58.9	59.1	60.3	60.0
Phenol	39.1	39.3	37.9	38.4
m-cresol, o-cresol	ND[3]	ND	ND	ND
Pyrocatechol	ND	ND	ND	ND
Cyclohexane	NA[4]	NA	NA	NA

Notes:

[1]Guaiacol conversion = $((C_{guaiacol,\ in} - C_{guaiacol,\ out})/(C_{guaiacol,\ in})) \times 100$

[2]TOF = $\frac{\text{Guaiacol flowrate (μmol per s) x conversion}}{\text{CO uptake (μmol per g) x catalyst weight (g)}}$

[3]ND = Not detected

[4]NA = Not analyzed

The activity versus temperature is reported in the next figure. There is a small amount of deactivation, but the activity reaches a constant value.

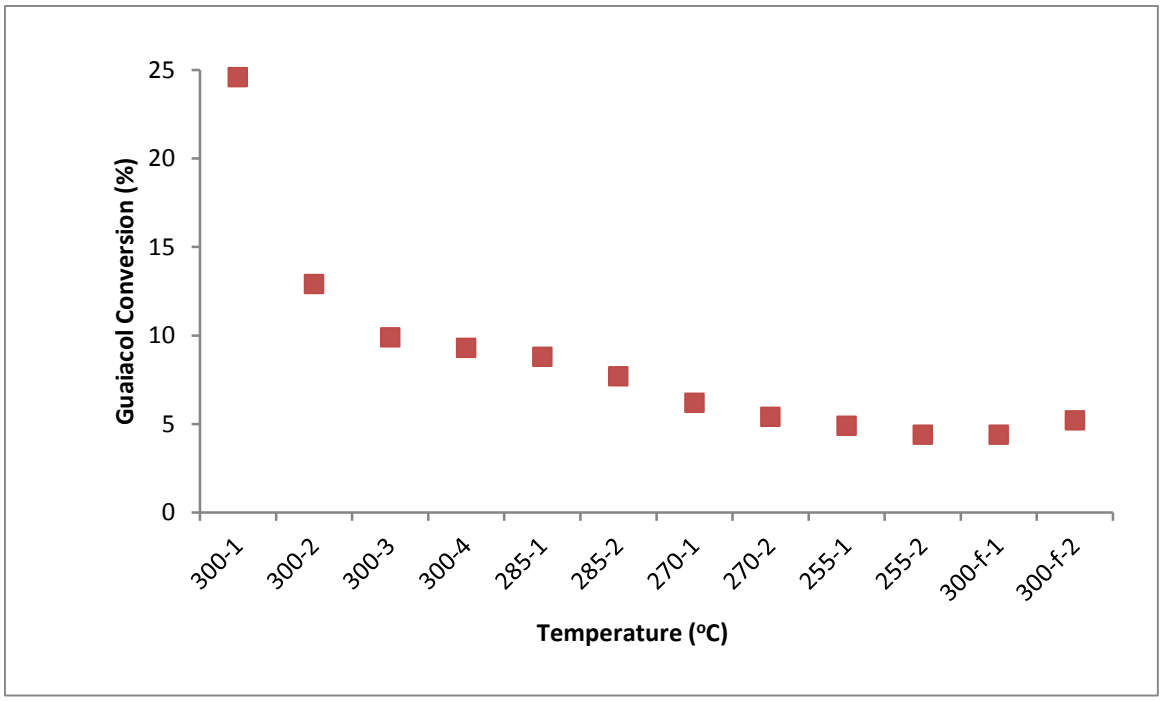

Figure 1. Conversion of guaiacol as a function of temperature over $Ni_2P/SiO2$ catalyst for guaiacol hydrodeoxygenation reaction. The reaction conditions have been given in Table 1.

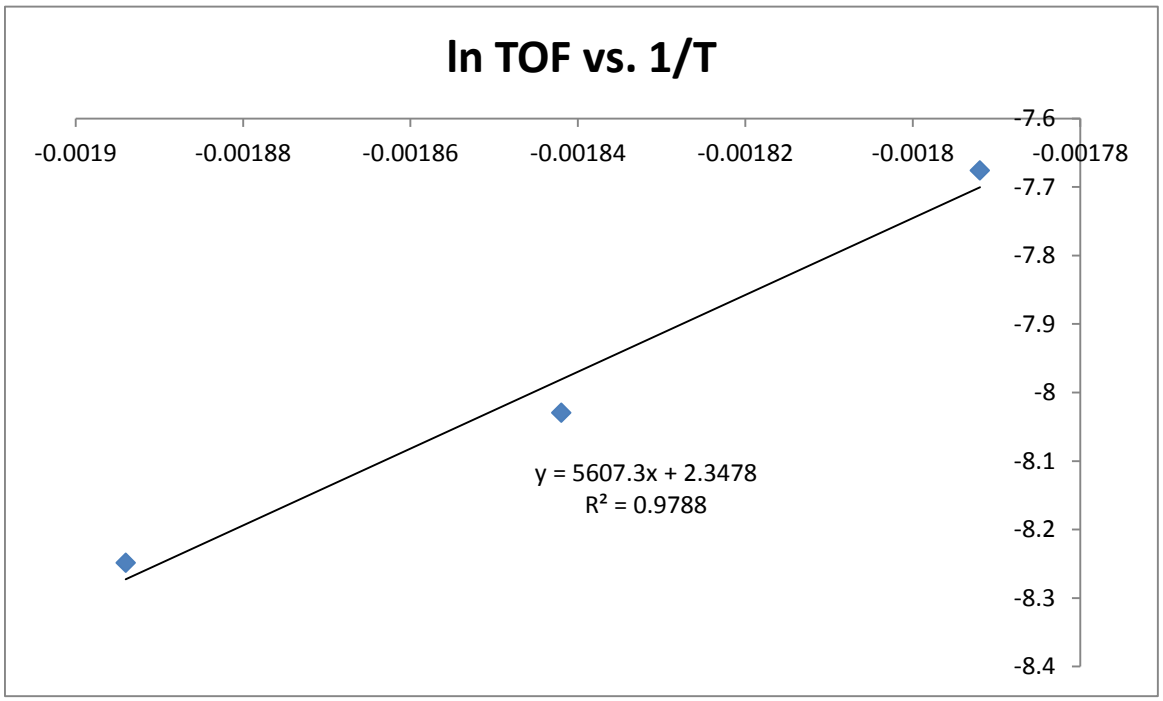

Figure 2. Plot of ln (TOF) vs. (1/T) for the calculation of apparent activation energy, E_a.

Task number: B. Operation of catalytic fluidized-bed reactors and product analysis (Agblevor)

1. **Planned Activities**:

B1.Preliminary studies on single stage reactor
B2.Construction and testing of two-stage reactor
B3.Bio-oil characterization
B.4 Catalytic pyrolysis studies in two-stage reactor

2. **Actual Accomplishments**:

The goals of this section of the project were to evaluate both commercial and new catalysts synthesized in Task A in both the existing single-stage fluidized bed pyrolysis reactor and the two-stage fluidized bed pyrolysis reactor. We designed and constructed the two-stage pyrolysis reactor and pyrolyze woody biomass feedstocks in this reactor and compared the results with those from the single-stage reactor. During the life of the project all planned activities were accomplished on time. For all the studies conducted in both the two-stage and single-stage reactors, hybrid poplar wood was used. Commercial catalysts were supplied by BASF Inc and these were evaluated in both the single stage and two stage reactors. The new catalysts synthesized in Task A were also evaluated in the two reactors. The bio-oils were characterized for new catalysts and commercial catalysts. For model compound studies, cellulose, hemicellulose and lignin samples were studied.

B1. Preliminary studies in the single-stage reactor

B1.1. Biomass Feedstock

Hybrid poplar wood samples were air dried and ground to pass a 1-mm screen in a Wiley mill prior to all experiments. The moisture content was determined using an HG53 Halogen Moisture analyzer (Mettler Toledo, Greifensee, Switzerland). The elemental composition and calorific value of the hybrid poplar wood shown in Table 1 was performed by Galbraith Analytical Laboratory (Knoxville, TN, USA).

Table 2.1. Elemental composition of hybrid poplar wood (moisture free basis)

Sample	Elemental Composition (wt %)						HHV(MJ/kg)
	C	H	O	N	S	Cl	
Hybrid Poplar	49.3	5.69	44.07	< 0.5	< 0.05	34 ppm	18.4

B1.2. Pyrolysis studies

The pyrolysis setup for the single-stage reactor studies is shown in Fig 2.1. This consisted of a screw-feeder, BASF Inc, supplied several FCC cracking catalysts with different zeolite contents and acidity. The catalysts are listed in Table 2.2 with code names to avoid revealing proprietary information to the public. These catalysts were used to pyrolyzed hybrid poplar wood described above and the products were characterized using ^{13}C-NMR and other tools. In addition, the pyrolysis oils were blended standard gas oil co-processed to determine the influence of the pyrolysis oils on the processing of the standard gas oil.

The pyrolysis product yields are shown in Table 2.2 and the simulated distillation curves of the various products are shown in Fig 2.2. The ^{13}C-NMR of the products are also shown for some of the products in Fig 2.4. Clearly, it can be concluded that stable biomass pyrolysis oils were produced that have unique properties. These oils are distillable and are very stable over

time. This is the first time that such an oil fraction has be produced anywhere in the world. The co-processed oils showed elimination of the residual oxygen in the oils.

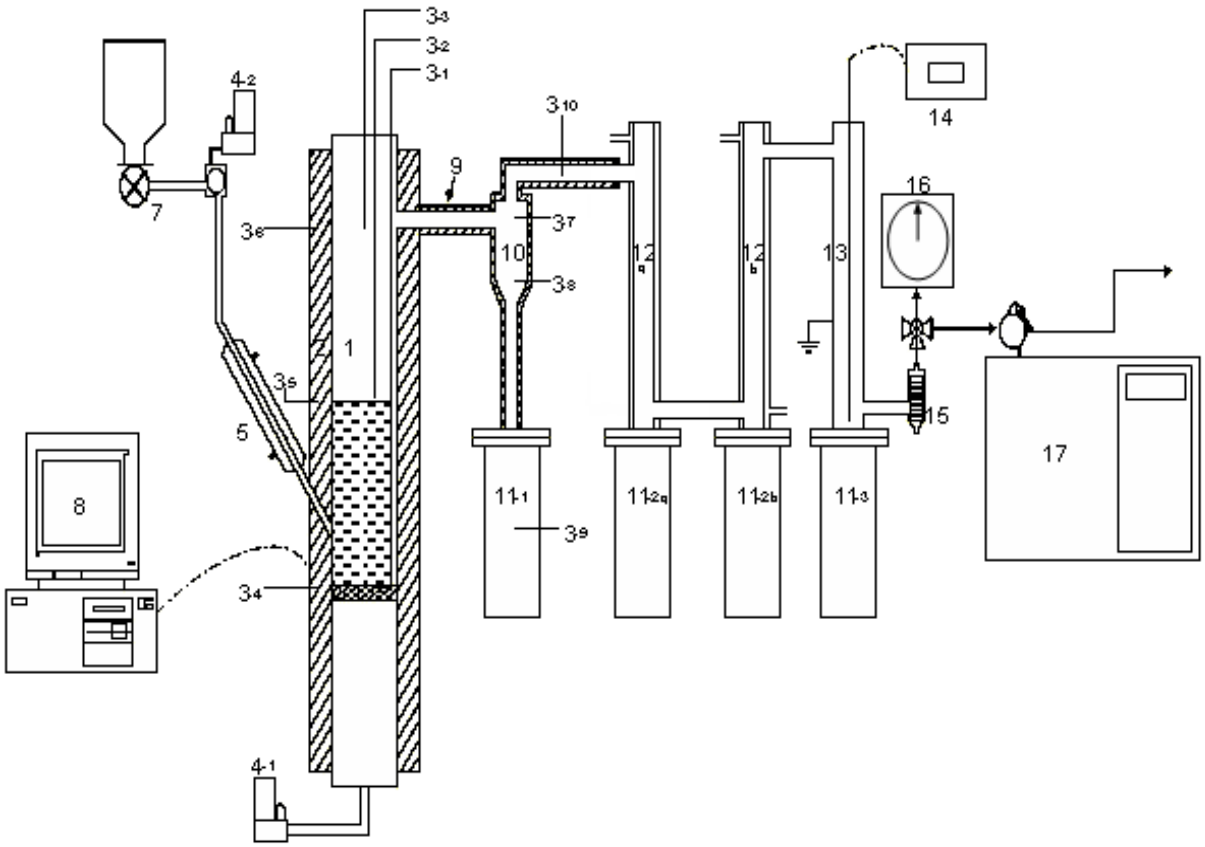

Fig 2.1. Schematic diagram of single-stage fluidized bed pyrolysis reactor set up.

Table 2.2. Pyrolysis products yield distribution using various catalysts					
Type of Catalyst	Type of Reactor	Product Yield Distribution			
		Water (wt.%)	Organics (wt.%)	Char (wt.%)	Gas (wt.%)
FCC- (<63 µm)	Bench scale	31.64	23.16	16.10	29.1
MBC-1(355µm)	Bench scale	12.74	30.16	16.62	40.48
MBC-2(283µm)	Bench scale	22.62	28.74	13.46	35.18
MBC-3(124µm)	Bench scale	21.86	33.21	13.41	31.52
BASF VP11(<63 µm)	Bench scale	20.53	38.17	14.13	27.17
BASF VP12(<63 µm)	Bench Scale	27.27	31.47	13.72	27.54
BASF VP13(<63 µm)	Bench scale	28.99	29.36	14.87	26.78
BASF VP14(<63 µm)	Bench scale	42.67	27.62	16.67	13.04
BASF VP15 (<63 µm)	Bench scale	31.13	34.64	14.54	19.69
BASF VP16(124 µm)	Bench scale	21.86	30.47	20.13	27.54

Table 2.3. Physical properties of biomass pyrolysis oils produced using various catalysts					
Type of Catalyst	Type of Reactor	Physical Properties of oil from ESP			
		pH	Density (g/cm^3)	Dynamic Viscosity (50^oC) (cP)	Water content (wt. %)
FCC- (<70 µm)	Bench scale	3.58	1.221	357.0	4.43
MBC-1(355µm)	Bench scale	2.92	1.188	333.0	3.47
MBC-2(283µm)	Bench scale	2.53	1.192	306.5	2.43
MBC-3(124µm)	Bench scale	2.53	1.201	348.5	3.30
BASF VP11(<63 µm)	Bench scale	2.98	1.184	197.0	3.10
BASF VP12(<63 µm)	Bench Scale	3.01	1.210	325.0	2.50
BASF VP13(<63 µm)	Bench scale	3.24	1.194	276.0	3.60
BASF VP14(<63 µm)	Bench scale	3.29	1.211	365.4	3.50
BASF VP15 (<63 µm)	Bench scale	3.14	1.190	286.0	3.56
BASF VP16(124 µm)	Bench scale	2.78	1.200	318.0	2.02

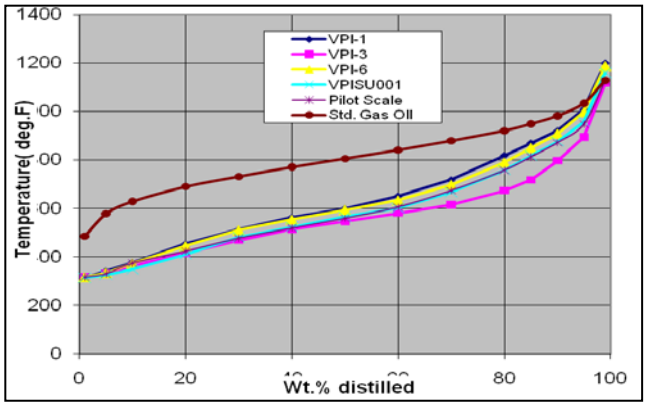

Fig 2.2. Simulated distillation curves of pyrolysis oils using various catalysts.

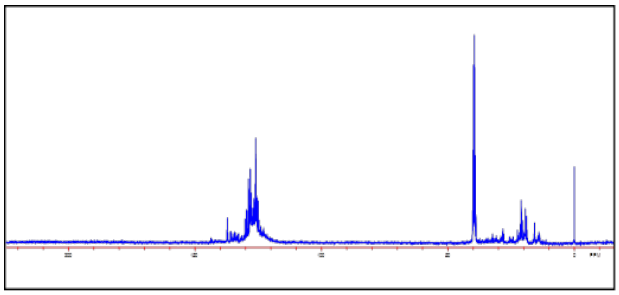

Fig 2.3. ^{13}C-NMR of co-processed oils.

The effect of gas recycling on the performance of various catalysts was also investigated. We observed that the recycled gases increased the yield of liquid products slightly and influenced the composition of the final gas products. The hydrocarbon and methane fractions of the gas products increased relative to the process without recycle.

B2. Construction and testing of two-stage pyrolysis reactor.

The two-stage reactor was designed and constructed for use in the catalytic pyrolysis. Fig 2.3. shows the schematic drawing of the reactor compared to the single-stage reactor. Prelimnary testing and CFD evaluation of the reactor were performed and the reactor performed according to specification. Biomass pyrolysis results are discussed in section B4.

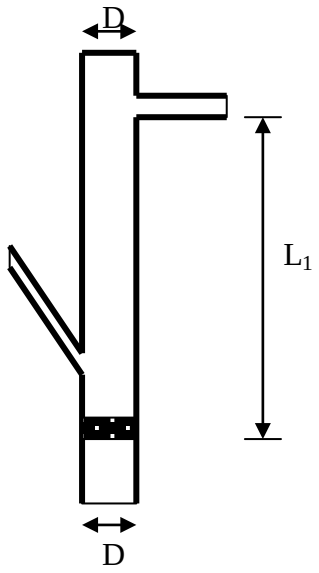

Figure 2.4a. 1-stage fluid bed reactor

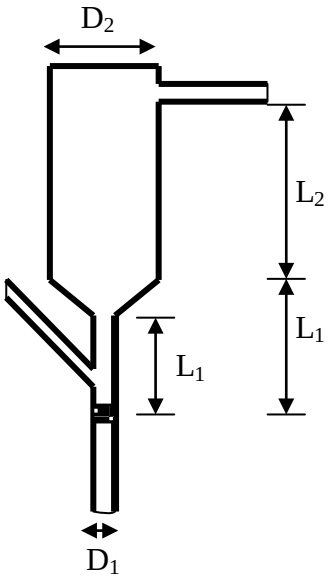

Figure 2.4b. 2-stage fluid bed reactor

B3. Characterization of biooils

The catalytic pyrolysis oils were characterized using Karl Fischer titration, total acid number, (TAN), viscometric analysis, aging studies, ^{13}C-NMR, FTIR, and GPC. The Karl Fischer analysis showed that the catalytic pyrolysis generates a large amount of water and subsequently reducing the organic fraction yield considerably lower than the non-catalytic pyrolysis oils.

We observed that ASTM method for total acid number determination for biomass pyrolysis oils was long and tedious and so we developed a new and rapid method for quantifying the total acid number. With this new method, we showed that the TAN for the catalytic oils was 41 compared to 90 for the non-catalytic pyrolysis oils. The oils produced from this process were more stable than the conventional non-catalytic pyrolysis oils and they had very low viscosity and flowed freely (Fig 2.5). The storage studies showed the viscosity of the stable pyrolysis oils did not change much with storage time under ambient conditions (Fig 2.6).
The ^{13}C-NMR studies showed that the catalyst converted most of the carbohydrate decomposition products to gases and other compounds (Fig 2.7.) whiles most of the lignin decomposition products were preserved. Thus, the oil using multiple catalysts was rich in phenols.

The gel permeation chromatographic (GPC) analysis of the catalytic pyrolysis oils showed a narrow molecular weight distribution (Fig 2.8) due to the effective cracking of the polymers by the catalyst which explains the low viscosity of the oils.

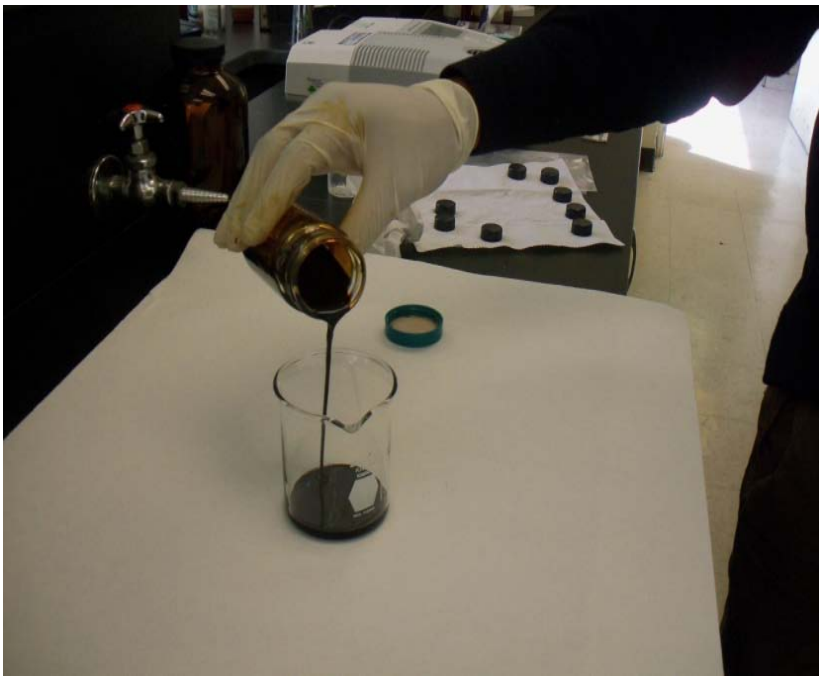

Fig 2.5. Photo of hybrid poplar catalytic pyrolysis oil showing very low viscosity of the oil.

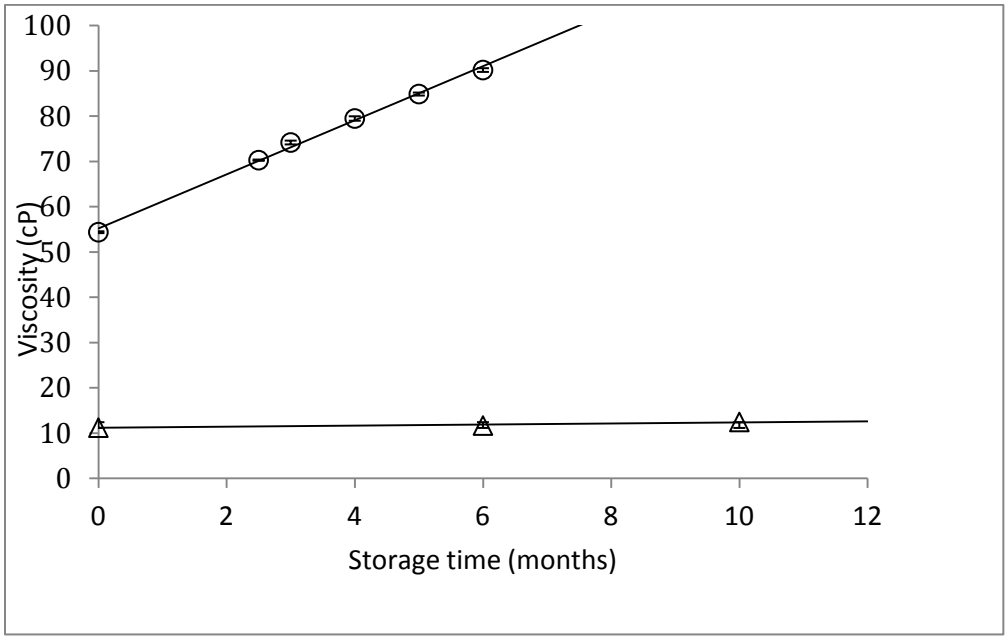

Fig 2.6. Influence of storage time on viscosity of oils. Δ FCP Oils; o RP oils.

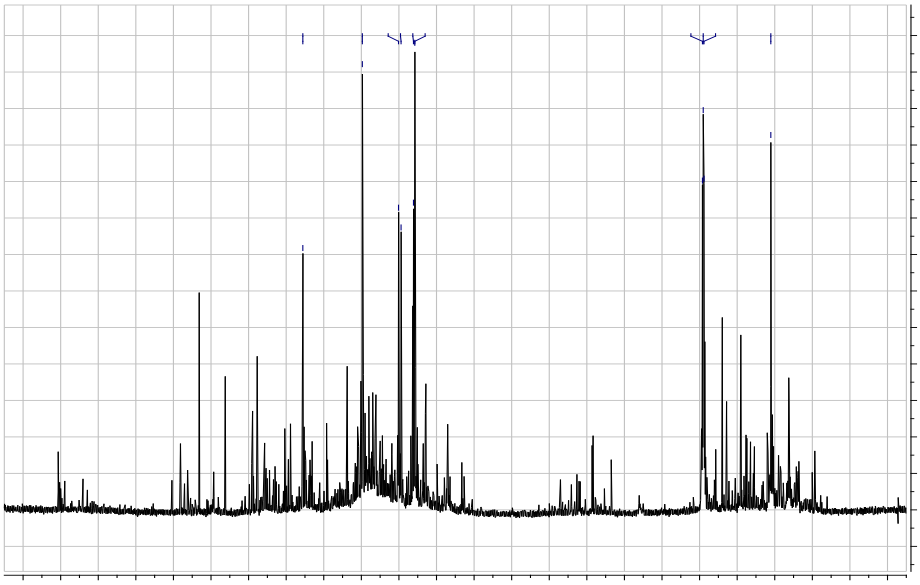

Fig 2.7. A typical ^{13}C-NMR spectrum of hybrid poplar catalytic pyrolysis oil.

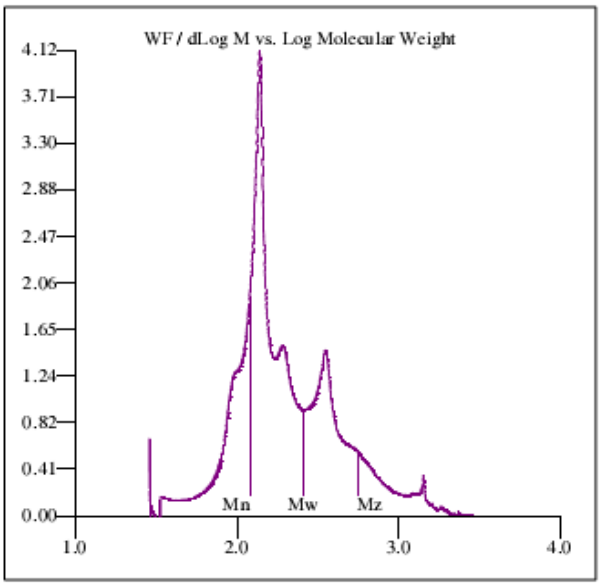

Fig 2.8. Molecular weight distribution of catalytic pyrolysis oil M_n = 120; M_w = 257;M_z = 555; M_p = 134; and M_n/M_w = 2.136

B4. Catalytic pyrolysis studies in two-stage reactor

The catalyst used for the trials were commercially available fluid cracking catalysts (FCC) and l ZSM-5 FCC based additives. The catalysts were supplied and characterized by BASF Catalysts LLC (Iselin, NJ, USA). The catalysts were mildly steamed at 732.2 ^{o}C with 100% steam for 4 hours in a fluidized bed reactor to stimulate a commercial deactivation process so that its performance was representative of an equilibrium catalyst. Both fresh and steamed forms of the catalyst were tested. The multipoint BET method was used to determine the total surface areas of the various catalysts. The measurements were based on the isothermal adsorption of nitrogen in accordance to the procedure described in ASTM D3663 using a Micrometrics TriStar instrument. The data from the multipoint determination was used to calculate the matrix surface area using the t-plot method. The difference between the BET surface area and the matrix surface was considered to be the zeolite surface area. The characteristics of the FCC catalyst and the ZSM-5 based additive are shown in Table 2. The ZSM-5 additive was blended into the FCC catalyst at 25 wt%, 50 wt% and 75 wt% level. The FCC catalyst had higher BET surface area compared to the ZSMS-5 additive. The steamed FCC catalyst contained about 40% of Y-zeolite and the ZSM-5 additive had about 13% ZSM-5 zeolite. Hence the addition of ZSM-5 additive to FCC catalyst will decrease the BET surface areas and consequently lower the aggregate activity of the blend catalysts.

Table 2.4. Catalysts used for the two-stage pyrolysis reactor studies

Catalyst	TSA (m^2/g)	MSA (m^2/g)	ZSA (m^2/g)	APS (µm)
Fresh FCC	516	112	404	108
Steamed FCC	391	104	287	102
Fresh ZSM-5 additive	141	45	96	91
Steamed ZSM-5 additive	120	27	93	86

B4.1. Fractional catalytic pyrolysis

The fractional catalytic pyrolysis of hybrid poplar was carried out using a bench scale pyrolysis unit. The unit consisted of a K-Tron volumetric feeder (K-Tron Process Group, Pitman, NJ), a fluidized bed reactor, hot gas filter, two chilled water condensers, an electrostatic precipitator and a coalescing filter. The 1-stage fluid bed reactor (Figure 2.9a) is a 20-in tall 316 stainless steel pipe, 2-in (D_1) in diameter and a reactor height (L_1) of 12-in. The 2-stage fluid bed reactor was constructed also from 316 stainless steel pipe consisting of a small diameter section of 0.75-in (D_1) and large diameter section of 2.5 (D_2). The reactor height of the small section is 5.5-in (L_1) and that of the large section is 7.5-in (L_2). The reactors were equipped with 100 µm distribution plate. Each reactor was externally heated with a three-zone electric furnace (Thermcraft, Winston-Salem, NC) and the temperatures were measured and controlled by three K-thermocouples inserted into a thermal well in the reactors. 250 g of biomass was charged into the feed hopper and was continuously fed for an hour into a hot bed of FCC catalyst and blends containing 25, 50, 75 wt.% ZSM-5 additives at 475-500 ^{o}C. The weight hourly space velocity (WHSV) for each experiment was 2.0 h^{-1}. The catalytic media was fluidized with 6.5 L/min of nitrogen gas to ensure intimate and uniform contact between the feed and the catalyst throughout the reactor as well as to minimize the losses of fine catalyst into the hot gas filter. The apparent average total vapor residence time was approximately 6 s for the single stage and 6.5 s for the two-stage reactor. The apparent average total vapor residence time was defined as the total volume of fluidized catalyst divided by gas flow rate at reactor conditions.

The mixture of char, entrained catalyst, gases and vapors that exited the reactor was separated by a hot gas filter maintained at 380 °C. The separated gases and vapors were then passed through two condensers connected in series. The condensers were maintained at average temperature of −8 °C with a 50/50 cooling mixture of ethylene glycol and water from an 18-L refrigerated circulating bath (Haake, Karlsruhe, Germany). Any condensable gases and aerosols that escaped from the condenser were captured by an electrostatic precipitator (ESP) kept at 16–20 kV. The temperatures across the reactor, hot gas filter and the condensers were controlled and monitored using an Omega multiscan (1200) acquisition system with TempView 2.1 program. The nitrogen gas flow rate was controlled by a mass flow controller and the total non-condensable gas that exited the coalescing filter was measured with a totalizer. The evolved gases were analyzed every 3.25 minutes online by a micro gas chromatography (Varian 490-GC). The micro GC is equipped with two modules, a 10m Molsieve (MS) 5Å column and a 10m porous polymer (PPU) column. Each module is equipped with a thermal conductivity detector. The MS column was used to analyze hydrogen, methane and carbon monoxide. Carbon dioxide and C_1-C_5 gases were analyzed by the PPU column. The mass of char/coke was determined gravimetrically by weighing the hot gas filter and the reactor before and after each pyrolysis experiment. The total mass of bio-oil was also determined gravimetrically by weighing the condensers and electrostatic precipitator before and after each experiment. The total mass of the non-condensable gas was calculated from the average gas composition and the total volume of the non-condensable gases.

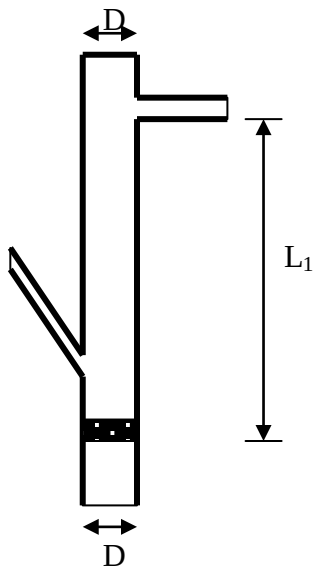

Figure 2.9a. 1- stage fluid bed reactor

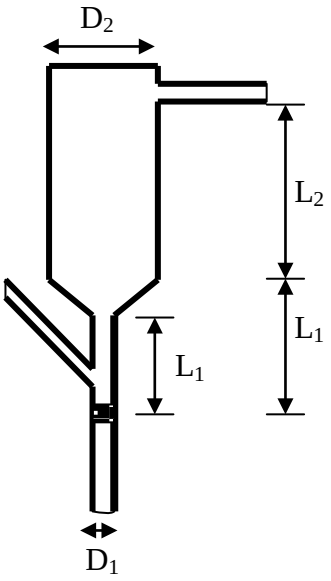

Figure 2.9b. 2-stage fluid bed reactor

B4.2. Bio-oil Analysis

A Thermo Scientific Flash 2000 organic elemental analyzer was used to determine the C, H, N, O, and S of the bio-oil fraction. The higher heating values (HHV) were determined using IKA C2000 basic bomb calorimeter (IKA® Works, Inc, NC, and U.S.A.) according to ASTM D2015. The pH was measured using a Mettler Toledo pH Meter and probe (Mettler-Toledo GmbH, Switzerland). The pH data were obtained after 15 min stabilization of the mechanically stirred oil. The viscosity and density of the bio-oils were measured at 40 ^{o}C with a SVM 3000 Stabinger viscometer (Anton Parr, Graz, Austria). The results were equivalent to

viscosities determined by the ASTM D445 method. A Metrohm 701KF Titrino (Brinkmann Instruments, Inc, N.Y, U.S.A) and a 703 titration stand setup were used for the Volumetric Karl Fischer titration. Hydranal® Composite 5 reagent was used and 50ml of methanol were used as solvent. About 60-100 mg of oil sample was loaded into a hypodermic plastic syringe and weighed. The sample was injected into the titration solvent and the syringe was weighed again. The water content was titrated volumetrically and the resulting mass was recorded.

The ^{13}CNMR spectra were recorded on a JOEL 300 MHz NMR spectrometer. About 1.0 g of oil was dissolved in 0.7 ml of dimethyl sulfoxide-d_6 in a 5mm sample tube. The NMR solvent, DMSO-d_6 [99.9 atom % D, contain 1% (v/v) tetramethylsilane (TMS)] was obtained from Sigma-Aldrich. The observing frequency for the ^{13}C nucleus was 100.58MHz. The pulse width was 10 µs, the acquisition time was 1.58 s, and the relaxation delay was 2 s. The spectra were obtained with 4000 scans and a sweep width of 20.0 KHz.

B4.3. Results and Discussion

The influence of reactor configuration on the fractional catalytic pyrolysis process was investigated using 1-stage and 2-stage fluid bed reactors. The 1-stage had the same fluidizing bed diameter across the length of reactor but the 2-stage reactor was designed with varying fluidizing bed diameters. The 2-stage reactor configuration would allow pyrolysis to occur at a shorter contact-time in the first stage of the reactor since the gas velocity in the small diameter section will be relatively higher. The large section of the 2-stage reactor would experience lower gas velocity and catalytic cracking would predominately be expected to occur in that section at a longer time.

The figures shown in 2.10a and 2.10b respectfully represent a typical temperature and gas flow profile for the 1-stage and the 2-stage reactor. The temperature profile depicts the different types of reactions that were occurring over the period of the experiment. Each reactor was equipped with three thermocouples for measuring temperatures at the bottom, middle and top of the reactor. For the 2-stage reactor, the bottom thermocouple (T_1) measured the temperature in the small section and both middle (T_2) and top thermocouples (T_3) measured the temperature across the large section of the reactor. The temperature program for the T_1 and T_2 of the reactor were set to 500 ^{o}C and T_3 at 475 ^{o}C to prevent further cracking of the vapors.

From the profiles, it can be seen that the temperature behavior in the 1-stage reactor was different from that of the 2-stage reactor. For a well-mixed bed, it is expected that at least two of the three thermocouples will indicate about the same temperature. The fluidizing gas flow rate of 6.5 L/min corresponded to about $12U_{mf}$ in the 1-stage reactor. The 2-stage reactor had gas velocities of $87.5U_{mf}$ and $7.9U_{mf}$ in the small and large sections respectively. For the 1-stage reactor, a uniform sinusoidal pattern for the T_1 and T_2 thermocouples that measured the bottom and middle part of the reactor was observed. However, the two-stage reactor showed separate temperature profiles for the thermocouples in the small and large sections. The T_1 thermocouple showed a lower temperature profile when compared to T_2 which showed relatively higher temperature profile. This suggests that, the small and large sections were operating at different reaction regimes. It appeared that endothermic reactions primarily occurred in the 1-stage of the reactor and endothermic reactions took place in the second stage. This may also imply that the initiation (homogenous) reaction which is pyrolytic/thermal was decoupled from the catalytic (heterogeneous) reaction to some extent in the 2-stage reactor. It is worth noting that these different reaction regimes shown by the temperature profiles observed in the 2-stage reactor were not evident in the single reactor. Nevertheless, the temperature profile for T_1 of the 1-stage reactor and T_1 of the 2-stage reactor were of similar sinusoidal patterns.

The reactor configuration also played a role in the loss of catalyst into the hot gas filter during the experiment. Table 2.5 shows the change in reactor content after the experimental runs. The values that exceed 100 % implies that there was an increase in the reactor content due to accumulation of larger char particles and values less than 100 % suggest the loss of

catalyst. It is clear from table 3 that the 2-stage reactor experienced up to 30 % loss of catalyst. The nature of the fluidized bed (bubbling, turbulent and spouting) obviously depends on the superficial gas velocity in the reactor. The superficial gas velocity in the 1-stage reactor was approximately 0.049 m/s and the gas velocities in the 2-stage reactor were 0.35 m/s (small section) and 0.0315 m/s (large section).

Higher superficial velocity in the reactor will increase catalyst entrainment and result in catalyst carry over into the hot gas filter. Therefore, it appeared that the higher gas velocity (0.35 m/s) in the small section of the 2-stage reactor may have caused entrainment of catalyst fines such that the lower gas velocity in the large section was insufficient to prevent catalyst losses.

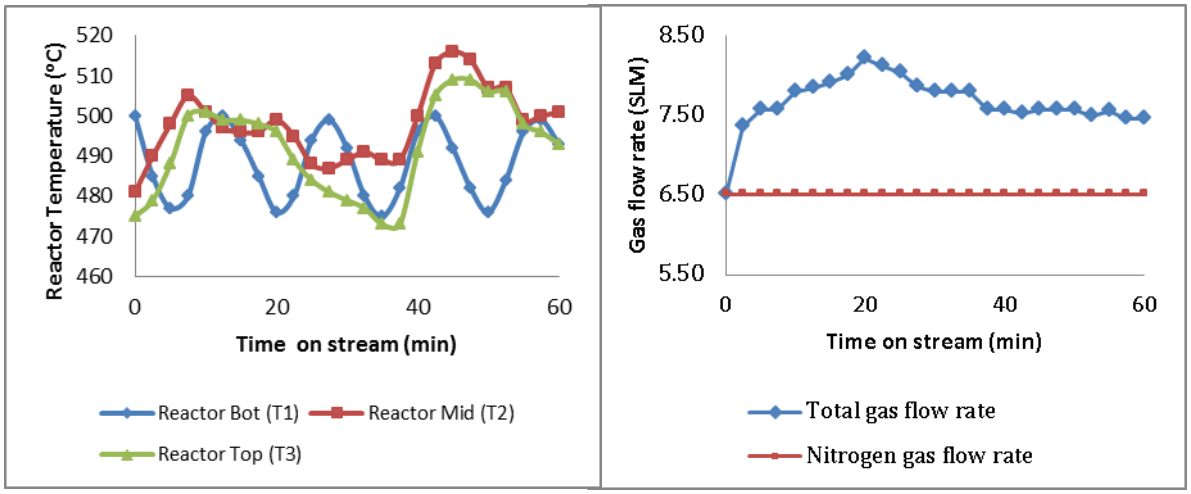

Figure 2.10. a) Typical temperature and gas flow profiles for the 1-stage reactor

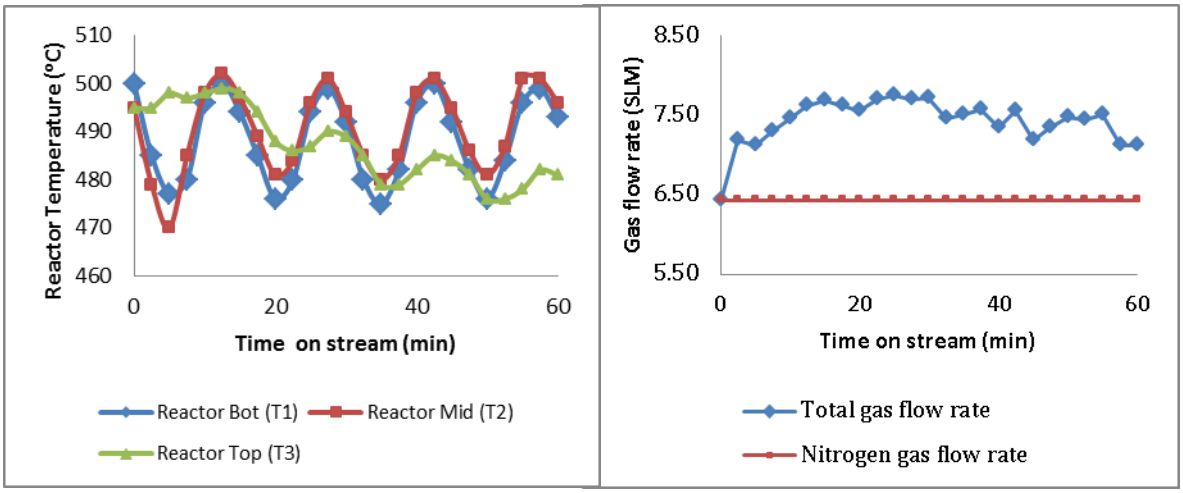

Figure 2.10b. Typical temperature and gas flow profiles for the 2-stage reactor

Table 2.5. Effect of reactor configuration on catalyst losses

Type of Catalyst	Change in reactor content after run (%)	
	1-stage reactor	2-stage reactor
FCC	112.6	75.5
75% FCC & 25% ZSM-5	113.0	69.2
50% FCC & 50% ZSM-5	109.0	71.6
25% FCC & 75% ZSM-5	102.0	69.5
ZSM-5	101.5	69.8

B4.3.1. Product distribution

The product distribution plots in figure 2.11 shows the effect of the addition of ZSM-5 additive to the base FCC catalyst in the fractional catalytic pyrolysis of hybrid poplar wood. In the 1-stage reactor experiment using fresh catalyst, the base FCC catalyst gave an organic yield of 13.8 wt% but increased to 19.4 wt% when the blend catalyst had 50 wt% of ZSM-5 additive. The char/coke yield consequently decreased from 26.6 wt% to 21.0 wt%. The addition of ZSM-5 at 50 wt% level resulted in about 40% increase in organic and 21% decrease in char/coke yields. The results from the 1-stage reactor using steamed catalyst showed similar trends in the product distribution. However, the steamed catalyst produced relatively higher yields of organics and lower yields of char/coke. The organic yield increased from 15.5 wt% to 24.2 wt% and the char/coke yield decreased from 24.1 wt% to 19.7 wt% at 50 wt% level of ZSM-5 additive. A further increase in the ZSM-5 additive to 75 wt% level in the blend catalyst did not result in any appreciable effect. The increase in organic yield at a 50 wt% and 75 wt% additive levels relative to the base FCC catalyst were respectfully 56.7% and 63.1%. It appeared that the influence of ZSM-5 additive at higher addition levels on the organic yields was subdued by the contributing effect of catalyst steaming. A Similar effect was observed in the char/coke yield. The addition of 25 wt% ZSM-5 additive to the base FCC catalyst resulted in about 22% decrease in char/coke yields. Nonetheless, a further increase of ZSM-5 additive at 50-75 wt% levels accounted for an additional 4% decrease. These results again indicate that steaming of the catalyst had confounding effect on the product yields at high ZSM-5 additive levels. Steaming typically reduces the catalyst activity which consequently decreases the intrinsic coke forming tendency of the catalyst.

The product distribution from the 2-stage reactor using the steamed catalyst was quite different. In comparison, the FCC catalyst produced higher organic yield (17.4 wt%) in the 2-stage reactor than in the 1-stage reactor (13.45 wt%). The organic yield from the 2-stage reactor was expected to have been lower since secondary vapor cracking could occur as a result of the high temperature and relatively longer vapor residence time in the large section. However, the observed effect was contradictory to what was presumed. The possible reason for the higher organic and lower char/coke yield produced by the steamed FCC catalyst in the 2-stage could be as a result of the relative lower concentration of catalyst in the reactor. It was shown in Table 3 that the use of the 2-stage reactor resulted in about 30% loss of catalyst into the hot gas filter. The increase in catalyst losses during the experiment decreases the catalyst concentration in the reactor and subsequently reduces the cumulative catalytic effect. This also implies that the actual WHSV in the 2-stage reactor would be higher. In comparison to the 1-stage reactor, there was negligible loss of catalyst. Hence, the relative catalytic effect would be higher (lower WHSV). This explains the lower organic yield and higher char/coke yield produced with the base FCC catalyst in the 1-stage reactor when compared with the 2-stage reactor.

The effect of the blend catalyst on the product yields from the 2-stage reactor also followed similar trends as seen with the 1-stage experiment. The organic yields increased and the char/coke yields decreased with increase in ZSM-5 additive level. The water and gas yields were not affected much with the use of ZSM-5 additive. However, the increase in ZSM-5 additive showed a gradual decrease in gas yields whilst there was no observed trend in the water yield. It is worth noting that the effect of the ZSM-5 additive in the 2-stage reactor was not

as intense as reported for the 1-stage reactor. For instance, at a 75 wt% ZSM-5 additive level, the organic yield increased by 29% and 63.1% respectively for the 2-stage and the 1-stage reactor. Additionally, the same catalyst blend caused 11.5% decrease in char/coke for the 2-stage reactor compared with a decrease of 24. 6% in the char/coke yield for the 1-stage reactor. The difference in the measure of influence by the ZSM-5 additive on the product distribution between the two reactors was attributed partly to process conditions due to reactor configuration and different reaction regimes experienced in the reactors.

Generally, the product slate for the fractional catalytic pyrolysis of hybrid poplar wood was dependent on the type of catalyst and the reactor configuration. The effect of the ZSM-5 additive was predominantly on the organic and char/coke yields. The decrease in the char/coke yield with the use of ZSM-5 additive was attributed to the reduction in coke formation. The decrease in the formation of coke was due to the characteristic narrow pore size of the ZSM-5 zeolite in the catalyst blends. The Y-zeolite in the FCC catalyst is considered to be highly active due to its acidity and large pore size [37, 40-42] whilst the ZSM-5 zeolite is known to be selective because of its narrow pores [2, 3, 7, 14, 22, 24, 58, 59]. The pore channels of the ZSM-5 zeolite are small such that it is difficult for coke precursors such as polyaromatics products to form [2, 25, 58]. The Y-zeolite on the other hand allows larger coke precursors to enter the pore structure leading to coke formation. Thus, the increase of ZSM-5 additive and the decrease of FCC catalyst in the blend resulted in a gradual reduction of coke and contributed to higher organic yields.

B4.3.2. Gas Analysis

The gas yield distribution shown in Table 4 was determined by a gas flow totalizer and gas chromatograph. The use of a micro gas chromatograph allowed timely analysis of the composition of the non-condensable gases during the experiment. The identified gases were H_2, CH_4, CO, CO_2 and C_2-C_5 hydrocarbons. The carbon oxides (CO_2 and CO) were the main gases produced in the catalytic vapor cracking of the oxygenated hydrocarbons and they constituted over 80% of the gas yields. The individual gas yields were influenced by the catalyst system and reactor configuration. Typical yields of CO were in the range of 13-15 wt% and that of CO_2 were between 9 -13 wt%. The C_1-C_5 hydrocarbons yields ranged between 5 – 6.2 wt% and H_2 was less than 0.5 wt%.

The FCC catalyst had higher selectivity for H_2, CH_4 and CO_2 and the ZSM-5 additive had higher selectivity for C_4 and C_5 hydrocarbons. Catalytic cracking of the vapors in the 2-stage reactor showed that the steamed FCC catalyst produced higher carbon oxides yield (27.86 wt%) compared with the steamed ZSM-5 additive (24.08 wt%). The most abundant light hydrocarbon gas produced with the FCC catalyst was CH_4 which accounted for about 40% of the total hydrocarbons. For ZSM-5-based additive and FCC/ZSM-5 additive blends, C_5s hydrocarbons were dominant.

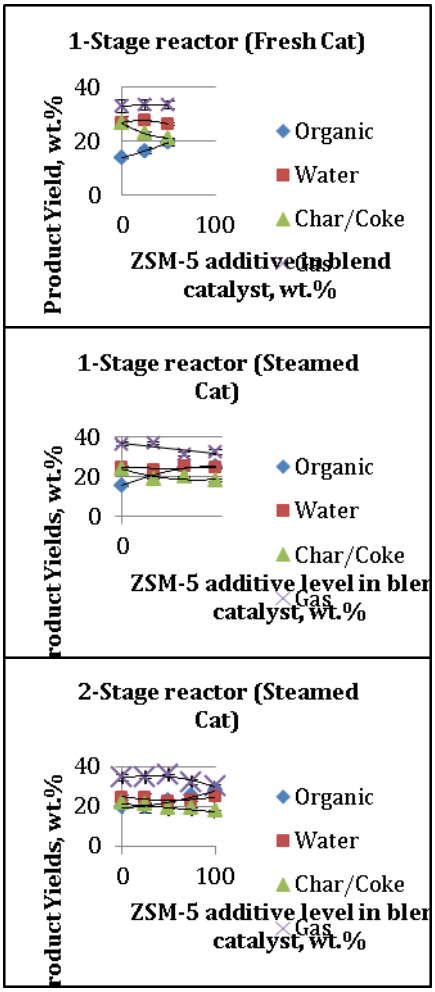

Figure 2.11. Effect of blending ZSM-5 additive with FCC catalyst on organic, water, char/coke and gas yields

The results from each reactor configuration evidently showed that the addition of ZSM-5 additive linearly decreased the selectivity for H_2, CH_4 and CO_2. The increase of ZSM-5 additive level in the FCC/ZSM-5 blend catalyst was found to specifically increase the selectivity for C_4 and C_5 hydrocarbons. The formation of CO was not essentially affected by the addition of ZSM-5 and did not also follow any particular trend. It can be inferred from the data that the ZSM-5 additive decreased decarboxylation reactions and increased reaction pathways for the production of C_4 and C_5 hydrocarbons.

The experiment with the FCC/ZSM-5 additive blend in the 2-stage reactor suggests interaction effect between the base FCC catalyst and the ZSM-5 additive on the formation of C_4 and C_5 hydrocarbons. Higher yields of C_5 hydrocarbons were generated with the FCC/ZSM-5 blends than the base FCC catalyst and the pure ZSM-5 additive. The highest yield of C_5 hydrocarbons was produced with the 25 % FCC and 75% ZSM-5 blend in the 1-stage reactor and the 50% FCC and 50% ZSM-5 blend in the 2-stage reactor. This suggests that the pure ZSM-5 additive was unable to convert some of the oxygenated hydrocarbons into C_4 and C_5 hydrocarbons due to its restricted small pore size. The presence of the large pore Y-zeolite (FCC catalyst) in the FCC/ZSM-5 blend probably cracked oxygenated hydrocarbons into smaller fragments and increased the amount of small hydrocarbons that could diffuse into the pore of

the ZSM-5 additive for conversion into C_4 and C_5 hydrocarbons. Hence, higher yields were relatively produced with the blend catalysts.

It is also important to note that the concentrations of the individual gases were affected by the reactor configuration as well as steaming of the catalyst. In the case of reactor configuration, it can be seen that most of the steamed catalyst blends gave slightly higher yields of H_2, CH_4 CO, CO_2, C_4 and C_5 hydrocarbons in the 2-stage reactor than in the 1-stage reactor. However, the C_2 and C_3 hydrocarbon gases were not influenced remarkably. The higher gas yields reported for the 2-stage reactor were probably due to extensive cracking of the pyrolysis vapors since the average temperature in the second section of the 2-stage reactor was slightly higher than what was experienced in the 1-stage reactor. Studies on zeolite catalytic cracking have shown generally that higher temperature increases the yield of the gas products due to the occurrence of secondary cracking reactions [26, 60-64]. From the results, the most widely influenced gases were H_2 and C_4 hydrocarbons. Depending of the catalyst system, the yields of H_2 and C_4 hydrocarbons from the 2-stage reactor were respectively 17–53% and 6–64 % higher than those generated from the 1-stage reactor.

Table 2.6. Individual gas yields, (wt% of biomass)

Gases	100% FCC	75% FCC & 25% ZSM-5	50% FCC & 50% ZSM-5	25% FCC & 75% ZSM-5	100% ZSM-5
1-Stage Reactor (Fresh catalyst blends)					
H_2	**0.13**±0.01	**0.09**±0.01	**0.1**±0.01		
CH_4	**1.76**±0.26	**1.66**±0.19	**1.49**±0.25		
CO	**13.4**±0.23	**13.68**±0.15	**14.97**±0.52		
CO_2	**10.02**±0.41	**8.99**±0.14	**9.4**±0.41		
C_2s	**0.41**±0.017	**0.4**±0.02	**0.47**±0.02		
C_3s	**0.59**±0.024	**0.57**±0.027	**0.67**±0.03		
C_4s	**0.8**±0.12	**1.07**±0.08	**1.08**±0.1		
C_5s	**0.9**±0.27	**2.06**±0.1	**2.06**±0.37		
C_2-C_5	**2.7**±0.44	**4.1**±0.05	4.28±0.25		
1-Stage Reactor (Steamed catalyst blends)					
H_2	**0.23**±0.02	**0.16**±0.01	**0.12**±0.01	**0.13**±0.011	
CH_4	**2.22**±0.18	**1.59**±0.14	**1.44**±0.21	**1.43**±0.09	
CO	**14.56**±0.21	**13.71**±0.11	**13.62**±0.09	**13.72**±0.15	
CO_2	**12.42**±0.2	**10.01**±0.16	**9.31**±0.03	**9.41**±0.14	
C_2s	**0.46**±0.002	**0.44**±0.008	**0.43**±0.003	**0.41**±0.007	
C_3s	**0.66**±0.006	**0.63**±0.02	**0.61**±0.003	**0.58**±0.02	
C_4s	**0.98**±0.03	**1.26**±0.03	**1.38**±0.08	**1.27**±0.06	
C_5s	**0.77**±0.05	**1.59**±0.1	**1.63**±0.07	**1.95**±0.1	
C_2-C_5	**2.87**±0.11	**3.92**±0.15	**4.05**±0.13	**4.21**±0.21	
2-Stage Reactor (Steamed catalyst blends)					
H_2	**0.27**±0.019	**0.24**±0.016	**0.22**±0.019	**0.2**±0.02	**0.18**±0.014
CH_4	**1.92**±0.102	**1.86**±0.123	**1.66**±0.042	**1.52**±0.13	**1.25**±0.06
CO	**14.77**±0.17	**14.96**±0.02	**14.73**±0.23	**14.43**±0.029	**13.57**±0.19
CO_2	**13.09**±0.15	**12.08**±0.03	**11.29**±0.16	**10.88**±0.05	**10.51**±0.10
C_2s	**0.45**±0.007	**0.44**±0.003	**0.44**±0.005	**0.44**±0.006	**0.43**±0.008
C_3s	**0.65**±0.01	**0.66**±0.005	**0.62**±0.008	**0.62**±0.008	**0.61**±0.011
C_4s	**1.61**±0.1	**1.55**±0.05	**1.47**±0.05	**1.41**±0.024	**1.36**±0.056
C_5s	**0.95**±0.07	**1.58**±0.08	**1.98**±0.10	**1.69**±0.105	**1.6**±0.03
C_2-C_5	**3.66**±0.13	**4.23**±0.11	**4.51**±0.16	**4.16**±0.13	**4.0**±0.10

Furthermore, results from the 1-stage reactor where both steamed and fresh catalyst were used showed that steaming of the catalyst influenced it's selectivity and consequently increased the individual gas yields for H_2, CO CO_2 and C_4 hydrocarbons. Among the carbon oxides, CO_2 was affected the most. This suggests that the steamed FCC catalyst increased the selectivity for decarboxylation and hydrogen producing reactions. The influence on the gas yields was attributed to catalyst modification as result of the decomposition of the zeolite and collapse of the matrix during steaming. Steam treatment of FCC catalyst generates non-framework aluminum species (Lewis acid sites) [65-68] which affects the activity and selectivity of the catalyst [69, 70].

The complete chain of reactions that lead to the generation of non-condensable gases in catalytic cracking of oxygenated hydrocarbons is still unclear. Nonetheless, Corma et al.[32] proposed that H_2, CO and CO_2 are generated from reactions such as dehydration, decarbonylation, dehydrogenation, water-gas shift (WGS) and steam reforming of dehydrated species. They suggested that, light hydrocarbons are formed through repeated dehydrogenation/hydrogenation or hydrogen transfer reactions. As already seen from the results, the FCC catalyst and the ZSM-5-based additive generated different gas yields and the variations in the gas composition can be attributed to their catalytic characteristics. One of the major differences between the FCC catalyst and ZSM-5 additive is the catalyst pore size and structure. The Y-zeolite crystal in FCC catalyst has parallel channels with large openings (7.4 Å) and is able to allow large molecules to diffuse into and crack [37, 39, 42]. The ZSM-5 zeolite has three-dimensional system of intersecting channels with a medium pore size opening (5.5 Å) and admits selectively smaller molecules for conversion into mainly light hydrocarbon (olefins) and aromatics [2, 4, 7, 18, 25, 44].

The Y-zeolite of the FCC catalyst and the ZSM-5 also differ in their mechanisms for cracking hydrocarbons. Primarily, there are two main types of mechanisms that govern acid catalyzed cracking of hydrocarbons [71, 72]. They are namely bimolecular (classical) cracking which involves hydride transfer reactions[73] and monomolecular cracking which occur by formation of carbonium ions[74]. The monomolecular (non-classical) cracking proposed by Haag and Dessau [74] extensively occurs in medium pore shape selective zeolites (ZSM-5)[75-77] since bimolecular reaction intermediates cannot be formed in the narrow pores. However, both monomolecular and bimolecular cracking reactions occur in the Y-zeolite of the FCC catalyst due to its relatively large pore size[78]. In short, the FCC catalyst catalyzes mainly cracking and hydrogen transfer reactions [40, 77, 79-82] and the ZSM-5 additive promotes isomerization and shape selective cracking reactions [81].

The exact determination of the contribution of these cracking mechanism in the cracking of biomass pyrolysis vapors is impossible since most of the reactants are more than four carbons[72]. However, the relatively higher yields of H_2, and CH_4 produced by the FCC catalyst when compared to the ZSM-5 additive suggest that protolytic cracking (monomolecular mechanism) of oxygenated hydrocarbons was dominant in the FCC catalyst [72, 75]. The higher yields in C_5 hydrocarbons produced from the FCC/ZSM-5 additive blends also suggest that isomerization and shape selective cracking were enhanced and both hydrogen transfer reactions and bimolecular reactions were minimized with the addition of ZSM-5 additive.

B4.3.3. Physico-chemical properties of bio-oils

The physical properties of the bio-oils in Tables 2.7-2.9 show that the addition of ZSM-5 additive affected the characteristics of the bio-oil. The ZSM-5 additive resulted in marginal improvement of the quality of the bio-oils. The viscosity of the bio-oil was the most influenced physical property. The addition of ZSM-5 additive decreased the viscosity of the bio-oil. The increases in pH and higher heating value (HHV) were all minimal. The elemental analysis of the bio-oils also showed that there was small increase in carbon content and decrease in oxygen content with the addition of ZSM-5 additive. The decrease in the viscosity of the bio-oils was

attributed to an increase in the formation of smaller molecular weight compounds promoted by the presence of ZSM-5 additive. The slight increases in pH of the bio-oils caused by addition of the ZSM-5 additive suggest that oxygenated functionalities that contribute to the acidity of the bio-oil were reduced by the ZSM-5 additive.

Table 2.7. Physical properties of bio-oil produced from single stage reactor using fresh catalyst blends

Property	Bio-oils		
	FCC	75% FCC & 25% ZSM-5	50% FCC & 50% ZSM-5
Moisture (wt%)	3.23	2.87	2.90
pH	2.76	3.16	3.08
Density (g/cm^3)	1.172	1.162	1.158
Kinematic viscosity, at 40 ^{o}C(cSt)	82.2	66.8	62.24
Elemental composition, wt% (moisture free)			
C	67.78	70.28	68.67
H	6.54	6.18	6.20
N	0.178	0.231	0.254
O	25.50	23.31	24.88
HHV (MJ/kg)	28.49	29.24	28.66

It is worth noting that the bio-oils produced with the blends of FCC/ZSM-5 additive in some cases had higher pH, HHV and carbon content as well as lower viscosities than the bio-oils produced with pure FCC catalyst or pure ZSM-5 additive. For instance, the catalytic cracking of the vapors with the fresh catalyst blend (75 wt% of FCC and 25 wt% of ZSM-5) in the 1-stage reactor produced bio-oil with the highest quality (Table 2.7). The bio-oil had higher carbon content (70 wt%) and lower oxygen content (23 wt%). Also, the bio-oil had relatively higher HHV (29.24 MJ/kg), lower viscosity (66.8 cSt) and higher pH (3.16) compared to the other bio-oils produced. This observation shows some synergistic effect of the FCC catalyst and the ZSM-5 additive on the physical properties.

Table 2.8. Physical properties of bio-oil produced from 1- stage reactor using steamed catalyst blends

Property	Bio-oils			
	FCC	75% FCC & 25% ZSM-5	50% FCC & 50% ZSM-5	25% FCC & 75% ZSM-5
Moisture (wt%)	2.80	2.70	3.00	3.30
pH	2.73	2.95	3.12	3.06
Density (g/cm3)	1.17	1.16	1.16	1.16
Kinematic viscosity, at 40 ^{o}C(cSt)	67.6	55.0	49.8	52.4
Elemental composition, wt% (moisture free)				
C	67.36	67.27	68.14	65.61
H	6.52	6.39	6.40	6.20
N	0.21	0.18	0.19	0.18
O	25.91	26.16	25.27	28.01
HHV (MJ/kg)	27.41	27.27	27.68	26.32

The results from the steamed catalyst using the 1-stage reactor revealed that higher levels of ZSM-5 additive could decrease the carbon content and consequently lower the HHV (Table 6). The bio-oil produced with blend catalyst containing 75 wt% of ZSM-5 additive

respectively had carbon and oxygen contents of 65.6 % and 28.0% compared with 68.1% and 25.3% for bio-oil produced with 50 wt% of ZSM-5 additive. Nonetheless, the results from the 2-stage reactor did not show such effect and the properties of the bio-oils produced with the FCC/ZSM-5 additive blends were comparable (Table 2.9). This again shows that reactor configuration played a role in the catalytic cracking of the pyrolysis vapors. The most obvious physical property that was influenced by the usage of the 2-stage reactor was viscosity. The viscosities of the bio-oils produced with the 2-stage reactor were higher than the bio-oils generated in the 1-stage reactor. The higher viscosities reported for the bio-oils from the 2-stage reactor could partly be as a result of the relatively higher temperature and longer residence time experienced by the vapors in the upper section of the reactor. At such conditions, secondary reactions could be enhanced which may favor polymerization reactions resulting in an increase in the viscosity of the bio-oil.

Table 2.9. Physical properties of bio-oil produced from the 2- stage reactor using steamed catalyst blends

Property	**Bio-oils**				
	FCC	75% FCC & 25% ZSM-5	50% FCC & 50% ZSM-5	25% FCC & 75% ZSM-5	ZSM-5
Moisture (wt%)	2.01	2.26	3.10	2.90	3.05
pH	2.78	3.15	3.09	3.13	3.09
Density (g/cm^3)	1.17	1.16	1.16	1.16	1.16
Kinematic viscosity, at 40 ^{o}C(cSt)	172	146	120	128	144
Elemental composition, wt% (moisture free)					
C	66.97	67.29	67.44	67.61	66.63
H	6.33	6.41	6.47	6.50	6.44
N	0.19	0.20	0.18	0.19	0.17
O	26.50	26.10	25.91	25.69	26.76
HHV (MJ/kg)	27.95	28.45	28.18	28.36	28.35

The carbon-13 nuclear magnetic resonance (^{13}C-NMR) spectra of the bio-oils produced from the 2-stage reactor in Figure 4 show the effect of ZSM-5 additive on the various chemical function groups in the bio-oil. Table 8 summarizes the integration of the ^{13}C spectra of the whole bio-oil. The aliphatic hydrocarbons (0-50 ppm) carbon content was higher in bio-oil from the FCC catalyst (26.43%) compared to the bio-oil from ZSM-5 additive (19.03%). Conversely, the carbon content due to aromatics (125-160 ppm) such as aromatic hydrocarbons, olefins were higher in the pure ZSM-5 additive bio-oils (38.47%) than the FCC catalyst bio-oil (25.34%). This results agree with the knowledge that FCC catalyst favors the formation of aliphatics due to hydrogen transfer reactions and ZSM-5 zeolite produces more aromatics and olefins via isomerization, Diels-Alder and aldol condensation [32]. The carbon content indicative of sugars and anhydrosugars (57-105 ppm) from the decomposition of carbohydrates were lower in the FCC bio-oil (7.9%) and relatively higher in the ZSM-5 additive bio-oil (9.5%). This suggests that the FCC catalyst cracks more of the pyrolysis dehydration product of cellulose (levoglucosan). The methoxyl carbon content (55-57 ppm) and the guaiacyl/syrigyl aromatic carbon (105-125 ppm) which are revealing of methoxylated phenolics were more in the bio-oil produced with the FCC catalyst. Additionally, the carbonyl carbons (160-180 ppm) belonging to carboxylic acids (eg., formic, acetic, propionic, etc.) and carbonyl carbons (180-220 ppm) due to ketones and aldehydes were found to be less in the bio-oil fraction from the ZSM-5 additive.

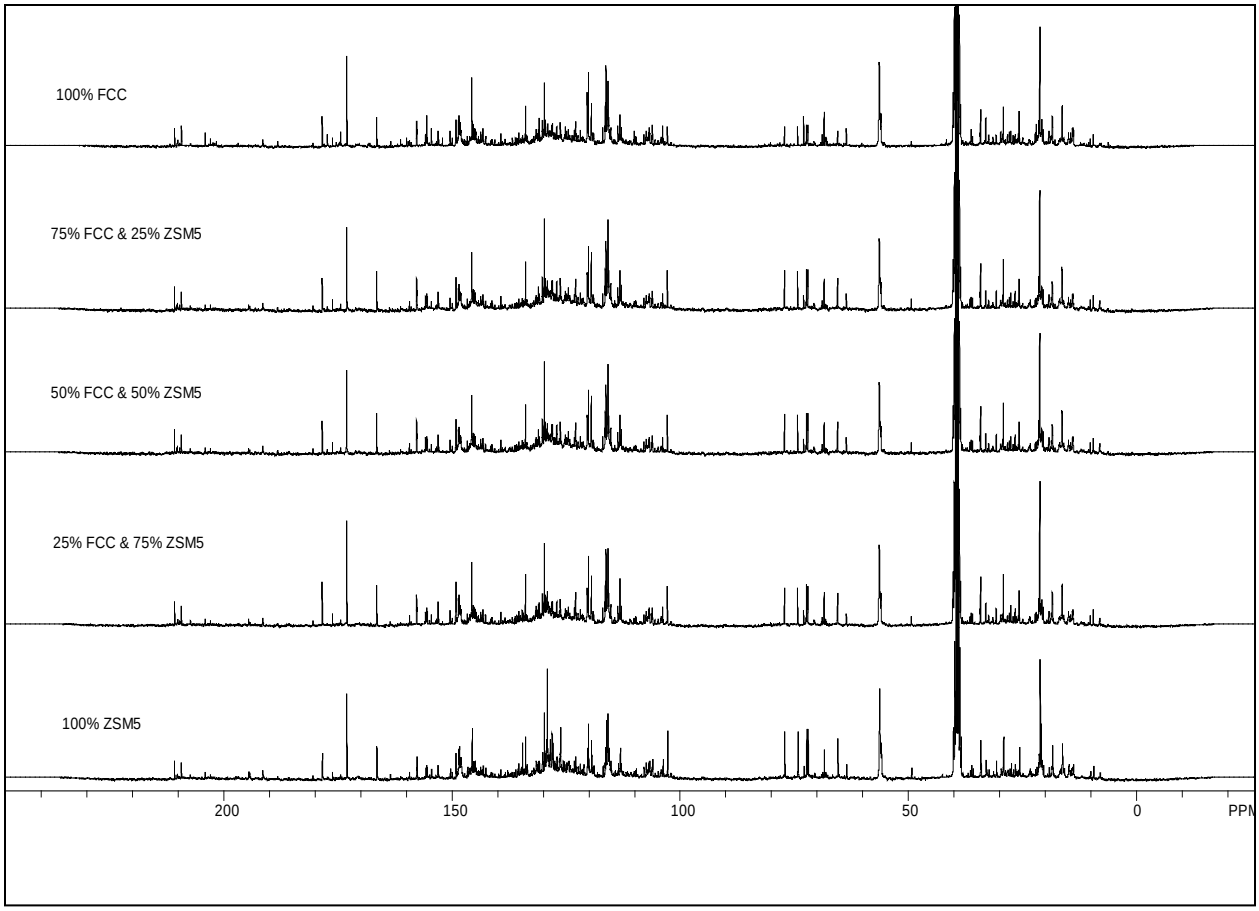

Figure 2.12. ^{13}C-NMR spectra of various whole bio-oil from two- stage reactor using steamed catalyst blends

The effect of ZSM-5 additive as a co-catalyst to FCC catalyst on the carbon distribution of the various chemical functionalities was reflective in the bio-oils produced with the FCC/ZSM-5 additive blends (see Tables 2.10 and 2.11). The increase in ZSM-5 additive corresponded to a gradual increase in aromatic hydrocarbons and a decrease in the aliphatic hydrocarbons for bio-oils produced with both 1-stage and 2-stage fluid bed reactors. The methoxylated carbons decreased in bio-oils produced with the 2-stage reactor but increased in bio-oils produced in the 1-stage reactor with the addition of ZSM-5 additive. Furthermore, the increase in ZSM-5 additive levels decreased carbon contents due to carboxylic acids, aldehydes and ketones in bio-oils from the 2-stage reactor. However, it appeared that the carbonyl functionalities in the bio-oils produced from the 1-stage reactor were not influenced by the addition of ZSM-5 additive. From the results, it is clear that the influence of ZSM-5 additive is dependent on the reactor configuration. Hence, the differences between the chemical compositions of the bio-oils produced in the 1-stage and the 2-stage is suggestive that some of the reactions that occurred in the reactors were dissimilar.

Table 2.10. ^{13}C-NMR Integration of whole bio-oil from 2- stage reactor using steamed catalyst blends

Chemical Shift region (ppm)	Type of Carbon	FCC	75% FCC & 25% ZSM-5	50% FCC & 50% ZSM-5	25% FCC & 75% ZSM-5	ZSM-5
0 - 50	Aliphatic hydrocarbon	26.43	24.29	24.81	23.76	19.03
55 - 57	Methoxyl	9.48	7.29	7.22	7.76	7.91
57 - 105	Levoglucosan, anhydrosugars, ethers, alcohols	7.97	8.67	8.62	8.52	9.47
105 - 125	Aromatic (guaiacyl, syringyl)	22.40	23.57	23.29	21.81	21.13
125 - 160	General Aromatic	25.34	29.34	29.39	32.50	38.47
160 - 180	Carbonyl (Carboxylic acids and derivatives)	5.55	4.35	4.22	3.95	3.51
180 - 220	Carbonyl (Aldehydes, Ketones)	2.83	2.48	2.45	2.47	1.61

Table 2.11. ^{13}C-NMR Integration of whole bio-oil from 1- stage reactor using steamed catalyst blends

Chemical Shift region (ppm)	Type of Carbon	FCC	75% FCC & 25% ZSM-5	50% FCC & 50% ZSM-5	25% FCC & 75% ZSM-5
0 - 50	Aliphatic hydrocarbon	27.32	25.81	23.42	20.76
55 - 57	Methoxyl	7.54	7.95	8.17	9.56
57 - 105	Levoglucosan, anhydrosugars, ethers, alcohols	6.24	5.17	6.67	5.37
105 - 125	Aromatic (guaiacyl, syringyl)	23.09	22.91	23.10	23.29
125 - 160	General Aromatic	29.15	31.78	32.71	33.43
160 - 180	Carbonyl (Carboxylic acids and its derivatives)	3.94	3.94	3.58	3.29
180 - 220	Carbonyl (Aldehydes, Ketones)	2.72	2.43	2.36	2.13

B4.3.4. CONCLUSIONS

The use of FCC catalyst in the catalytic pyrolysis of biomass results in large amount of coke and produces lower yields of bio-oil. In the present study, ZSM-5 based additive was investigated as a co catalyst to FCC catalyst in the fractional catalytic pyrolysis of hybrid poplar wood in a 1-stage reactor and a 2-stage reactor. From the experimental results reported, the addition of ZSM-5 additive increased the yield of bio-oil and decreased coke formation. The ZSM-5 additive influenced the composition of the non-condensable gases as well. The formation of H_2, CH_4 and CO_2 decreased and the generation of C_4-C_5 hydrocarbons increased with increasing levels of ZSM-5 additive in the blend catalyst. The use of the 1-stage and 2-stage fluid bed reactors showed that reactor configuration potentially influences the fractional catalytic pyrolysis.

The physical characteristics of the bio-oil fractions showed that the FCC/ZSM-5 additive blend catalyst produced bio-oils with improved oil properties when compared to the base catalyst (FCC). There was a decrease in acidity and viscosity as well as an increase in the higher heating value (HHV). The elemental analysis of the bio-oils showed that the fresh catalyst blend of 75 wt% of FCC and 25 wt% of ZSM-5 produced bio-oil with the highest carbon

content. The physical properties of the bio-oils and he gas composition of the non-condensable gases suggested some synergistic effect of the FCC catalyst and the ZSM-5 additive. Under the conditions used for the experiments, the ^{13}C-NMR spectrometric analysis of the whole bio-oil fractions showed that the addition of ZSM-5 additive to FCC catalyst gradually decreased the aliphatic hydrocarbon carbons and increased the aromatic hydrocarbon carbon content. The effect of ZSM-5 on the cracking of levoglucosan, carbonyl functionalities and methoxylated compounds from the decomposition of lignin were dependent on the configuration of the reactor. The bio-oils produced with the 2-stage reactor showed that ZSM-5 additive decreased the amount of methoxylated phenols and carbonyl groups belong to carboxylic acids, ketones and aldehydes.

REFERENCES

1. Adam, J., et al., *In situ catalytic upgrading of biomass derived fast pyrolysis vapours in a fixed bed reactor using mesoporous materials.* Microporous and Mesoporous Materials, 2006. **96**(1-3): p. 93-101.
2. Adjaye, J.D. and N.N. Bakhshi, *Production of hydrocarbons by catalytic upgrading of a fast pyrolysis bio-oil. Part II: Comparative catalyst performance and reaction pathways.* Fuel Processing Technology, 1995. **45**(3): p. 185-202.
3. Agblevor, F.A., et al., *Fractional Catalytic Pyrolysis of Hybrid Poplar Wood.* Industrial & Engineering Chemistry Research, 2010. **49**(8): p. 3533-3538.
4. Aho, A., et al., *Catalytic pyrolysis of woody biomass in a fluidized bed reactor: Influence of the zeolite structure.* Fuel, 2008. **87**(12): p. 2493-2501.
5. Ates, F., A.E. Pütün, and E. Pütün, *Fixed bed pyrolysis of Euphorbia rigida with different catalysts.* Energy Conversion and Management, 2005. **46**(3): p. 421-432.
6. Ates, F., A.E. Pütün, and E. Pütün, *Catalytic pyrolysis of perennial shrub, Euphorbia rigida in the water vapour atmosphere.* Journal of Analytical and Applied Pyrolysis, 2005. **73**(2): p. 299-304.
7. Carlson, T., et al., *Aromatic Production from Catalytic Fast Pyrolysis of Biomass-Derived Feedstocks.* Topics in Catalysis, 2009. **52**(3): p. 241-252.
8. Chen, N.Y., D.E. Walsh, and L.R. Koenig, *Fluidized-Bed Upgrading of Wood Pyrolysis Liquids and Related Compounds*, in *Pyrolysis Oils from Biomass*1988, American Chemical Society: Washington, DC. p. 277-289.
9. Iliopoulou, E.F., et al., *Catalytic conversion of biomass pyrolysis products by mesoporous materials: Effect of steam stability and acidity of Al-MCM-41 catalysts.* Chemical Engineering Journal, 2007. **134**(1-3): p. 51-57.
10. Lappas, A.A., D.K. Iatridis, and I.A. Vasalos, *Production of Liquid Biofuels in a Fluid Catalytic Cracking Pilot-Plant Unit Using Waxes Produced from a Biomass-to-Liquid (BTL) Process.* Industrial & Engineering Chemistry Research, 2010.
11. Lappas, A.A., et al., *Biomass pyrolysis in a circulating fluid bed reactor for the production of fuels and chemicals.* Fuel, 2002. **81**(16): p. 2087-2095.
12. Li, H.-y., Y.-j. Yan, and Z.-w. Ren, *Online upgrading of organic vapors from the fast pyrolysis of biomass.* Journal of Fuel Chemistry and Technology, 2008. **36**(6): p. 666-671.
13. Peng, J., et al., *Catalytic upgrading of bio-oil by HZSM-5 in sub- and super-critical ethanol.* Bioresource Technology, 2009. **100**(13): p. 3415-3418.
14. Pütün, E., B.B. Uzun, and A.E. Pütün, *Rapid Pyrolysis of Olive Residue. 2. Effect of Catalytic Upgrading of Pyrolysis Vapors in a Two-Stage Fixed-Bed Reactor.* Energy & Fuels, 2009. **23**(4): p. 2248-2258.
15. R. K. Sharma, N.N.B., *Catalytic upgrading of biomass-derived oils to transportation fuels and chemicals.* The Canadian Journal of Chemical Engineering, 1991. **69**(5): p. 1071-1081.

16. Radlein, D.S.A.G., et al., *Hydrocarbons from the catalytic pyrolysis of biomass.* Energy & Fuels, 1991. **5**(5): p. 760-763.
17. Ramesh K. Sharma, N.N.B., *Catalytic upgrading of fast pyrolysis oil over hzsm-5.* The Canadian Journal of Chemical Engineering, 1993. **71**(3): p. 383-391.
18. Samolada, M.C., A. Papafotica, and I.A. Vasalos, *Catalyst Evaluation for Catalytic Biomass Pyrolysis.* Energy & Fuels, 2000. **14**(6): p. 1161-1167.
19. Sharma, R.K. and N.N. Bakhshi, *Conversion of non-phenolic fraction of biomass-derived pyrolysis oil to hydrocarbon fuels over HZSM-5 using a dual reactor system.* Bioresource Technology, 1993. **45**(3): p. 195-203.
20. Srimat T. Srinivas, A.K.D.N.N.B., *Thermal and catalytic upgrading of a biomass-derived oil in a dual reaction system.* The Canadian Journal of Chemical Engineering, 2000. **78**(2): p. 343-354.
21. Vitolo, S., et al., *Catalytic upgrading of pyrolytic oils over HZSM-5 zeolite: behaviour of the catalyst when used in repeated upgrading-regenerating cycles.* Fuel, 2001. **80**(1): p. 17-26.
22. Vitolo, S., et al., *Catalytic upgrading of pyrolytic oils to fuel over different zeolites.* Fuel, 1999. **78**(10): p. 1147-1159.
23. Williams, P.T. and H.M. Chishti, *Two stage pyrolysis of oil shale using a zeolite catalyst.* Journal of Analytical and Applied Pyrolysis, 2000. **55**(2): p. 217-234.
24. Williams, P.T. and P.A. Horne, *Characterisation of oils from the fluidised bed pyrolysis of biomass with zeolite catalyst upgrading.* Biomass and Bioenergy, 1994. **7**(1-6): p. 223-236.
25. Williams, P.T. and P.A. Horne, *The influence of catalyst type on the composition of upgraded biomass pyrolysis oils.* Journal of Analytical and Applied Pyrolysis, 1995. **31**(1): p. 39-61.
26. Williams, P.T. and N. Nugranad, *Comparison of products from the pyrolysis and catalytic pyrolysis of rice husks.* Energy, 2000. **25**(6): p. 493-513.
27. Zhang, H., et al., *Comparison of non-catalytic and catalytic fast pyrolysis of corncob in a fluidized bed reactor.* Bioresource Technology, 2009. **100**(3): p. 1428-1434.
28. Zhang, H., et al., *Catalytic Fast Pyrolysis of Biomass in a Fluidized Bed with Fresh and Spent Fluidized Catalytic Cracking (FCC) Catalysts.* Energy & Fuels, 2009. **23**(12): p. 6199-6206.
29. Zhang, Q., et al., *Upgrading Bio-oil over Different Solid Catalysts.* Energy & Fuels, 2006. **20**(6): p. 2717-2720.
30. de Miguel Mercader, F., et al., *Production of advanced biofuels: Co-processing of upgraded pyrolysis oil in standard refinery units.* Applied Catalysis B: Environmental, 2010. **96**(1-2): p. 57-66.
31. Domine, M.E., et al., *Coprocessing of Oxygenated Biomass Compounds and Hydrocarbons for the Production of Sustainable Fuel.* ChemSusChem, 2008. **1**(3): p. 179-181.
32. Corma, A., et al., *Processing biomass-derived oxygenates in the oil refinery: Catalytic cracking (FCC) reaction pathways and role of catalyst.* Journal of Catalysis, 2007. **247**(2): p. 307-327.
33. Stöcker, M., *Biofuels and Biomass-To-Liquid Fuels in the Biorefinery: Catalytic Conversion of Lignocellulosic Biomass using Porous Materials.* Angewandte Chemie International Edition, 2008. **47**(48): p. 9200-9211.
34. Mante, O., F. Agblevor, and R. McClung, *Fluid catalytic cracking of biomass pyrolysis vapors.* Biomass Conversion and Biorefinery: p. 1-13.
35. Huber, George W. and A. Corma, *Synergies between Bio- and Oil Refineries for the Production of Fuels from Biomass.* Angewandte Chemie International Edition, 2007. **46**(38): p. 7184-7201.

36. de la Puente, G. and U. Sedran, *Conversion of methylcyclopentane on rare earth exchanged Y zeolite FCC catalysts.* Applied Catalysis A: General, 1996. **144**(1-2): p. 147-158.
37. Hosseinpour, N., et al., *Synergetic effects of Y-zeolite and amorphous silica-alumina as main FCC catalyst components on triisopropylbenzene cracking and coke formation.* Fuel Processing Technology, 2009. **90**(2): p. 171-179.
38. Fogassy, G., et al., *Biomass derived feedstock co-processing with vacuum gas oil for second-generation fuel production in FCC units.* Applied Catalysis B: Environmental, 2010. **96**(3-4): p. 476-485.
39. Tonetto, G.M., et al., *Effect of steaming treatment in the structure and reactivity of FCC catalysts.* AIChE Journal, 2006. **52**(2): p. 754-768.
40. Al-Khattaf, S., *The influence of Y-zeolite unit cell size on the performance of FCC catalysts during gas oil catalytic cracking.* Applied Catalysis A: General, 2002. **231**(1-2): p. 293-306.
41. Dight, L.B., Leskowicz, Mark A., Bogert, David C., *High zeolite content FCC catalysts and method for making them.*, 1990, ENGELHARD CORP (US).
42. Tonetto, G., J. Atias, and H. de Lasa, *FCC catalysts with different zeolite crystallite sizes: acidity, structural properties and reactivity.* Applied Catalysis A: General, 2004. **270**(1-2): p. 9-25.
43. French, R. and S. Czernik, *Catalytic pyrolysis of biomass for biofuels production.* Fuel Processing Technology, 2010. **91**(1): p. 25-32.
44. Lappas, A.A., S. Bezergianni, and I.A. Vasalos, *Production of biofuels via co-processing in conventional refining processes.* Catalysis Today, 2009. **145**(1-2): p. 55-62.
45. Graça, I., et al., *Catalytic cracking of mixtures of model bio-oil compounds and gasoil.* Applied Catalysis B: Environmental, 2009. **90**(3-4): p. 556-563.
46. Lee, K.-H., et al., *Thermal and catalytic degradation of waste high-density polyethylene (HDPE) using spent FCC catalyst.* Korean Journal of Chemical Engineering, 2003. **20**(4): p. 693-697.
47. Lee, K.-H. and D.-H. Shin, *A comparative study of liquid product on non-catalytic and catalytic degradation of waste plastics using spent FCC catalyst.* Korean Journal of Chemical Engineering, 2006. **23**(2): p. 209-215.
48. Li, H., et al., *Enhancing the production of biofuels from cottonseed oil by fixed-fluidized bed catalytic cracking.* Renewable Energy, 2009. **34**(4): p. 1033-1039.
49. Samolada, M.C., W. Baldauf, and I.A. Vasalos, *Production of a bio-gasoline by upgrading biomass flash pyrolysis liquids via hydrogen processing and catalytic cracking.* Fuel, 1998. **77**(14): p. 1667-1675.
50. Chew, T.L. and S. Bhatia, *Effect of catalyst additives on the production of biofuels from palm oil cracking in a transport riser reactor.* Bioresource Technology, 2009. **100**(9): p. 2540-2545.
51. Adewuyi, Y.G., D.J. Klocke, and J.S. Buchanan, *Effects of high-level additions of ZSM-5 to a fluid catalytic cracking (FCC) RE-USY catalyst.* Applied Catalysis A: General, 1995. **131**(1): p. 121-133.
52. Buchanan, J.S., *The chemistry of olefins production by ZSM-5 addition to catalytic cracking units.* Catalysis Today, 2000. **55**(3): p. 207-212.
53. Degnan, T.F., G.K. Chitnis, and P.H. Schipper, *History of ZSM-5 fluid catalytic cracking additive development at Mobil.* Microporous and Mesoporous Materials, 2000. **35-36**: p. 245-252.
54. Dzikh, I.P., et al., *Mixing effect of USHY+HZSM-5 for different catalyst ratios on the n-heptane transformation.* Applied Catalysis A: General, 1999. **176**(2): p. 239-250.

55. Zhao, X. and T.G. Roberie, *ZSM-5 Additive in Fluid Catalytic Cracking. 1. Effect of Additive Level and Temperature on Light Olefins and Gasoline Olefins.* Industrial & Engineering Chemistry Research, 1999. **38**(10): p. 3847-3853.
56. Li, X., et al., *Effects of large pore zeolite additions in the catalytic pyrolysis catalyst on the light olefins production.* Catalysis Today, 2007. **125**(3-4): p. 270-277.
57. Schipper, P.H., et al., *Zeolite ZSM-5 in Fluid Catalytic Cracking: Performance, Benefits, and Applications*, in *Fluid Catalytic Cracking*1988, American Chemical Society. p. 64-86.
58. Adjaye, J.D. and N.N. Bakhshi, *Production of hydrocarbons by catalytic upgrading of a fast pyrolysis bio-oil. Part I: Conversion over various catalysts.* Fuel Processing Technology, 1995. **45**(3): p. 161-183.
59. Gayubo, A.G., et al., *Olefin Production by Catalytic Transformation of Crude Bio-Oil in a Two-Step Process.* Industrial & Engineering Chemistry Research, 2009. **49**(1): p. 123-131.
60. Evans Robert, J. and T. Milne, *Molecular-Beam, Mass-Spectrometric Studies of Wood Vapor and Model Compounds over an HZSM?5 Catalyst*, in *Pyrolysis Oils from Biomass*1988, American Chemical Society. p. 311-327.
61. Mathews, J.F., et al., *Upgrading of aspen poplar wood oil over HZSM-5 zeolite catalyst.* The Canadian Journal of Chemical Engineering, 1985. **63**(4): p. 686-689.
62. Sharma, R.K. and N.N. Bakhshi, *Upgrading of wood-derived bio-oil over HZSM-5.* Bioresource Technology, 1991. **35**(1): p. 57-66.
63. Carlson, T.R., et al., *Production of green aromatics and olefins by catalytic fast pyrolysis of wood sawdust.* Energy & Environmental Science, 2011. **4**(1): p. 145-161.
64. Encinar, J.M., et al., *Catalytic pyrolysis of exhausted olive oil waste.* Journal of Analytical and Applied Pyrolysis, 2009. **85**(1-2): p. 197-203.
65. Katada, N., et al., *Acidic property of modified ultra stable Y zeolite: increase in catalytic activity for alkane cracking by treatment with ethylenediaminetetraacetic acid salt.* Journal of Molecular Catalysis A: Chemical, 2004. **211**(1-2): p. 119-130.
66. Narbeshuber, T.F., et al., *The influence of extraframework aluminum on H-FAU catalyzed cracking of light alkanes.* Applied Catalysis A: General, 1996. **146**(1): p. 119-129.
67. Wang, Q.L., G. Giannetto, and M. Guisnet, *Dealumination of zeolites III. Effect of extra-framework aluminum species on the activity, selectivity, and stability of Y zeolites in n-heptane cracking.* Journal of Catalysis, 1991. **130**(2): p. 471-482.
68. Williams, B.A., et al., *The roles of acid strength and pore diffusion in the enhanced cracking activity of steamed Y zeolites.* Applied Catalysis A: General, 1999. **177**(2): p. 161-175.
69. Beyerlein, R.A., et al., *Effect of steaming on the defect structure and acid catalysis of protonated zeolites.* Topics in Catalysis, 1997. **4**(1): p. 27-42.
70. Humphries, A., D.H. Harris, and P. O'Connor, *The Nature of Active Sites in Zeolites: Influence on Catalyst Performance*, in *Studies in Surface Science and Catalysis*1993, Elsevier. p. 41-82.
71. Corma, A., P.J. Miguel, and A.V. Orchillés, *Product selectivity effects during cracking of alkanes at very short and longer times on stream.* Applied Catalysis A: General, 1996. **138**(1): p. 57-73.
72. Corma, A. and A.V. Orchillés, *Current views on the mechanism of catalytic cracking.* Microporous and Mesoporous Materials, 2000. **35-36**: p. 21-30.
73. Greensfelder, B.S., H.H. Voge, and G.M. Good, *Catalytic and Thermal Cracking of Pure Hydrocarbons: Mechanisms of Reaction.* Industrial & Engineering Chemistry, 1949. **41**(11): p. 2573-2584.
74. Haag, W.O. and R.M. Dessau. in *Proceedings of the 8th International Congress on Catalysis*. 1984. Berlin: Verlag Chemie, Weinheim.

75. Jentoft, F.C. and B.C. Gates, *Solid-acid-catalyzed alkane cracking mechanisms: evidence from reactions of small probe molecules.* Topics in Catalysis, 1997. **4**(1): p. 1-13.
76. Jolly, S., et al., *Reaction mechanisms and kinetics in the n-hexane cracking over zeolites.* Applied Catalysis A: General, 1997. **156**(1): p. 71-96.
77. Corma, A., et al., *Light cracked naphtha processing: Controlling chemistry for maximum propylene production.* Catalysis Today, 2005. **107-108**(0): p. 699-706.
78. den Hollander, M.A., et al., *Synergy effects of ZSM-5 addition in fluid catalytic cracking of hydrotreated flashed distillate.* Applied Catalysis A: General, 2002. **223**(1-2): p. 103-119.
79. Scherzer, J., *Correlation Between Catalyst Formulation and Catalytic Properties*, in *Studies in Surface Science and Catalysis*1993, Elsevier. p. 145-182.
80. Zhao, X. and R.H. Harding, *ZSM-5 Additive in Fluid Catalytic Cracking. 2. Effect of Hydrogen Transfer Characteristics of the Base Cracking Catalysts and Feedstocks.* Industrial & Engineering Chemistry Research, 1999. **38**(10): p. 3854-3859.
81. Dwyer, F.G. and T.F. Degnan, *Chapter 13 Shape Selectivity in Catalytic Cracking*, in *Studies in Surface Science and Catalysis*, S.M. John and M.M. Maurice, Editors. 1993, Elsevier. p. 499-530.
82. de la Puente, G. and U. Sedran, *Evaluation of hydrogen transfer in FCC catalysts. A new approach for cyclohexene as a test reactant.* Chemical Engineering Science, 2000. **55**(4): p. 759-765.

Task number: C. Design and optimization of a two-stage fluidization unit (Battaglia)

1. **Planned Activities**:
   C.1.1 Test computational models
   C.1.2 Test simple geometry (one stage)
   C.1.3 Test-two stage geometry
   C.2.1 Validate with experiments
   C.2.2Perform parametric studies for adjustments
   C.2.3 Simulate final reactor design

2. **Actual Accomplishments**:

The simple (one-stage) reactor was modeled and simulated for the initial reactor design study. The catalyst particles were not perfectly spherical and validation was necessary to ensure that the drag force models predicted the correct physics. The BASF catalyst had a mean particle diameter of 0.63 μm and a very high coefficient of restitution (e = 0.9), which accounts for particle-particle interactions and the elasticity of the particles when they collide. The catalyst had a material density of approximately 2 g/cm^3 such that the Geldart classification of fluidized beds indicates that the catalyst is a Geldart A particle. The advantage of Geldart A particles is that they fluidize easily and the fluidization characteristics are similar to an aeratable bed. The caveat, however, is that if the inlet gas velocity is close to the minimum fluidization velocity, there will be regions of non-bubbling fluidization. At higher inlet gas velocities, the bed will produce a typical bubbling (fluidized) bed.

The minimum fluidization velocity and maximum pressure drop through the bed measured by the experiments was compared with the numerical simulations. The minimum fluidization velocity and maximum pressure drop were determined theoretically, which provided additional measures for validating both the experiments and numerical simulations. For the single stage reactor, the conditions modeled were for an initial particle bed height of 10.7 cm and bulk density of 0.82 g/cm^3; thus the initial void fraction (volume fraction of gas) was 0.6. The theoretical minimum fluidization velocity is 0.17 cm/s and maximum pressure drop is 864 Pa, assuming that the particle sphericity is 0.8 and the aforementioned bed conditions.

Experiments were conducted to determine the minimum fluidization velocity by increasing the flow rate and then decreasing the flow rate. As shown in Fig. 3.1 using circles, the experimental trends are very similar and indicate U_{mf} is approximately 8 cm/s. Comparable simulations were also performed based on the experimental conditions. It was determined that the Gidaspow drag force model best predicts the gas-solid hydrodynamics and performs well for a range of materials and will be employed in this study. The numerical predictions are in excellent agreement (shown in Fig. 3.1 as diamonds), indicating U_{mf} to be 8 cm/s as well. It should be noted that the theoretical minimum fluidization using the empirical relation of Eq. (1) is 7.72 cm/s. The pressure drop measured experimentally is 773 Pa, whereas the theoretical relation and the numerical predictions give a pressure drop of 645 Pa. Overall, the agreement is very good for this non-reacting flow.

Subsequently, the simulations were validated with the experiments for a binary mixture of sand and FCC particles. The first step was to compare the CFD predictions for pressure drop through the bed and minimum fluidization velocity with the experimental data. A better definition for minimum fluidization velocity U_{mf} was estimated using an improved correlation developed by Ergun (1952):

$$U_{mf} = \frac{\left(\psi d_p\right)^2 \left(\rho_p - \rho_g\right) g \varepsilon_g^3}{150 \mu_g \left(1 - \varepsilon_g\right)} \tag{3.1}$$

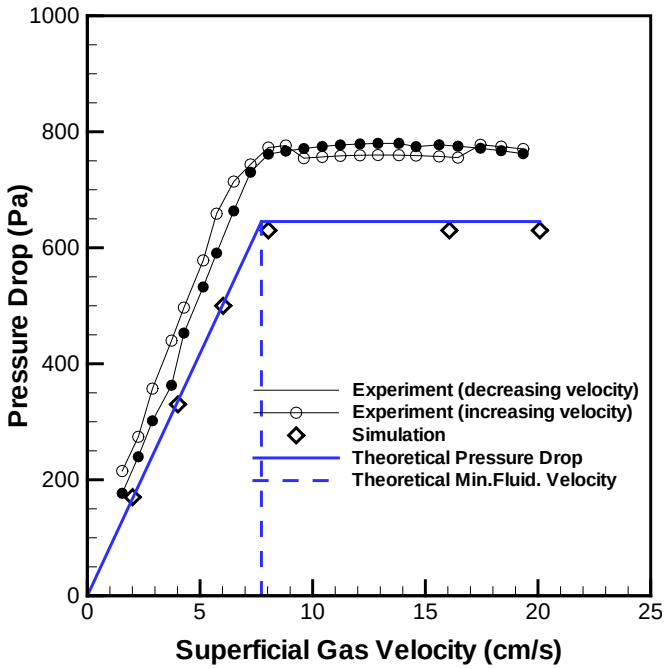

Figure 3.1 Pressure drop versus gas velocity for the non-reacting sand bed.

Equation 3.1 includes terms for the gas density ρ_g and viscosity μ_g, the particle sphericity ψ, mean diameter d_p and density ρ_p, respectively, the gas volume fraction ε_g and gravity g. The theoretical pressure drop through the bed of particles at the inception of fluidization is defined in terms of the weight of the particle bed prior to fluidization and the cross-sectional area of the reactor. Figure 3.2(a) shows a comparison of the experiments and CFD data for a binary mixture of 300 g sand and 200 g FCC particles. Both the CFD predictions and Ergun equation indicate that the binary bed begins to fluidize around 6.9 cm/s, consistent with the experiments. Furthermore, the corresponding pressure drop through the bed at fluidization reaches a constant value of approximately 1200 Pa. Overall, there is excellent agreement between the CFD and experiments.

Contours of instantaneous volume fractions are shown in Figure 3.3 for the (a) gas, (b) sand and (c) FCC. The void fraction (Fig. 3.3(a)) shows smaller gas bubbles rising and coalescing as they move upward. Although the segregation is not apparent in Fig. 3.1(b), the sand volume fraction (Fig. 3.3(b)) is very high at the bottom of the reactor with a fraction close to 65%. However, above 5 cm, there is more interaction between the sand and FCC, and segregation is not dominant as was the case for the simple reactor. The FCC still fluidizes very easily and small amounts are observed in the second stage of the reactor (between 20-35 cm). Based on this work, we hypothesized that the two-stage reactor improves mixing between the sand and FCC, which will be important for gasification. As will be shown, the FCC will initially react in the lower section of the reactor and will continue to react in the second stage.

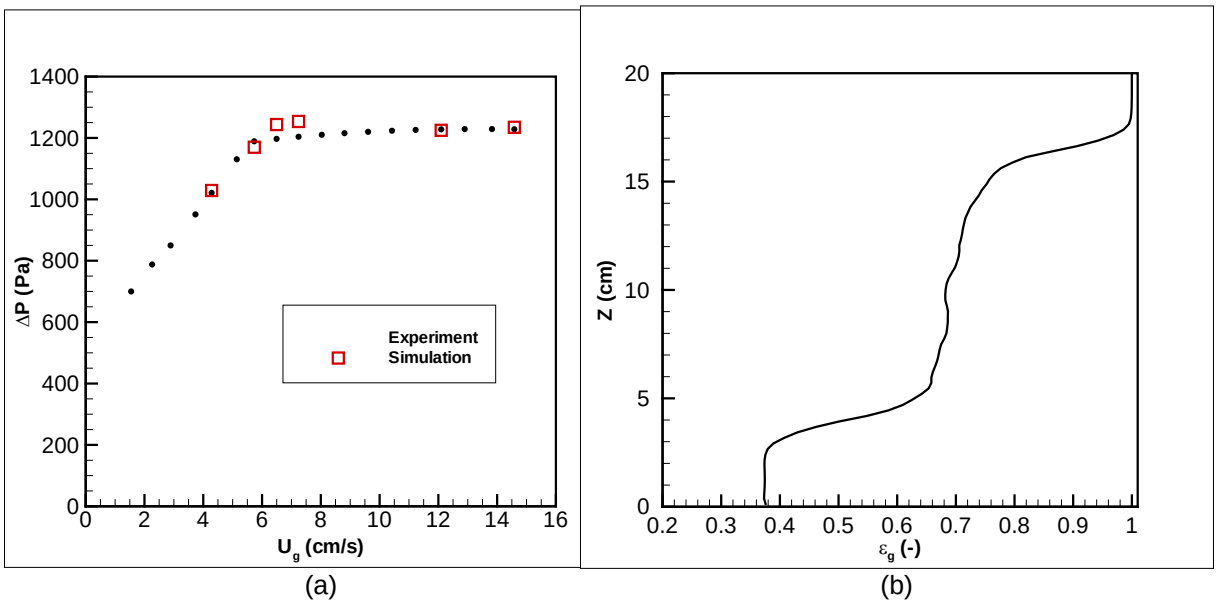

Figure 3.2 (a) Pressure drop versus inlet gas velocity comparing experiments and simulations. (b) Vertical position through the reactor versus void fraction from the CFD calculation.

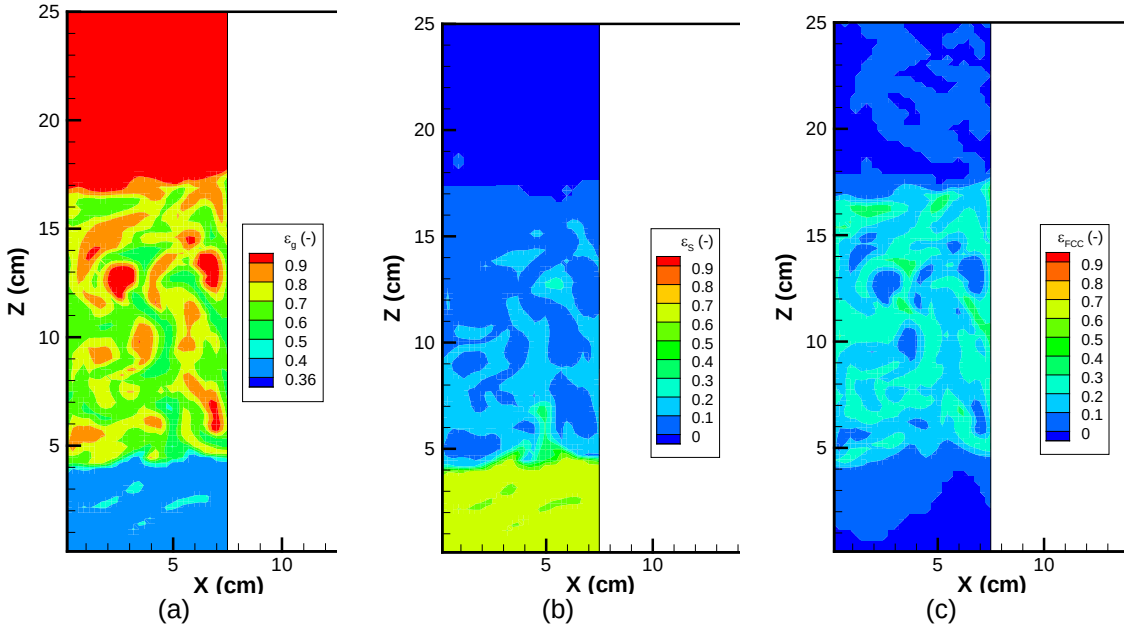

Figure 3.3. Instantaneous volume fraction contours for (a) gas, (b) sand and (c) FCC.

One of the key considerations in the operation of the two stage reactor is optimizing the segregation of the bed materials. It is desirable to have two distinct bed regions with one composed almost entirely of the inert bed material (lower region) and the other composed almost entirely of the active FCC bed material (upper region). The design of a two stage reactor is shown in Fig.3.4 and is a simplified schematic of Fig. 2.4b. By modeling the two stage reactor in MFIX it is possible to analyze the extent of segregation and determine the key parameters related to segregation.

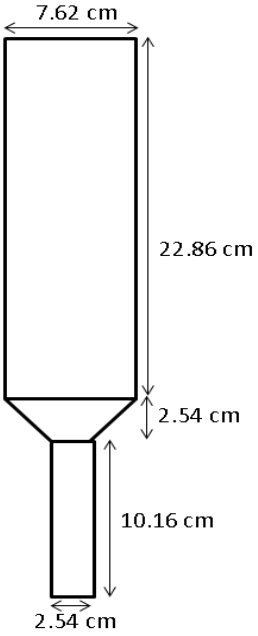

Fig. 3.4 Two stage reactor geometry

The first issue in the operation of the two stage reactor is determining appropriate amounts of bed material. In order to limit the expansion of the inert bed material (Kaolin) to only fluidize in the lower stage of the reactor, it was necessary to run several preliminary simulations with Kaolin only, as summarized in Table 3.1. For 36 g of Kaolin, the initial bed height was 8.0 cm and after fluidization the bed expanded to an average height of 11.9 cm. The bed expansion was too close to the second stage region of the reactor so the mass was decreased to 25 g. Using 25 g of Kaolin, the initial bed height was 6.0 cm and after the fluidization the bed expanded to an average height of 11.1 cm which was within the first stage region. Therefore, the mass of Kaolin for the remainder of the simulation studies will be fixed at 25 g.

The properties of Kaolin and FCC differ advantageously for the promotion of bed segregation. Kaolin has a larger diameter and higher density than the FCC, which should promote desirable size segregation of the Kaolin to the first stage (lower) region. These two materials can be classified using the Geldart classification, where Kaolin is a Geldart B particle that can fluidize reasonably well and FCC is Geldart A particle that easily fluidizes. The propensity for segregation can also be appreciated by examining the predicted individual minimum fluidization velocities U_{mf} of each material, where FCC fluidizes more readily at a lower velocity (see Table 3.1). Void fraction was used to demonstrate that the bed segregated, but it was necessary to examine individual particle volume fractions, as demonstrated by Fig. 3.5. At the expansion, it is obvious that Kaolin lies along the sloping side walls and FCC resides on top of the Kaolin.

Table 3.1. Particle properties for binary mixture.

Particle	Mass (g)	Diameter (μm)	Density (g/cm^3)	Bulk Density (g/cm^3)	U_{mf} (cm/s)
Kaolin	25	99.2	2.9	0.245	11.24
FCC	50	58.5	2.2	0.490	2.96

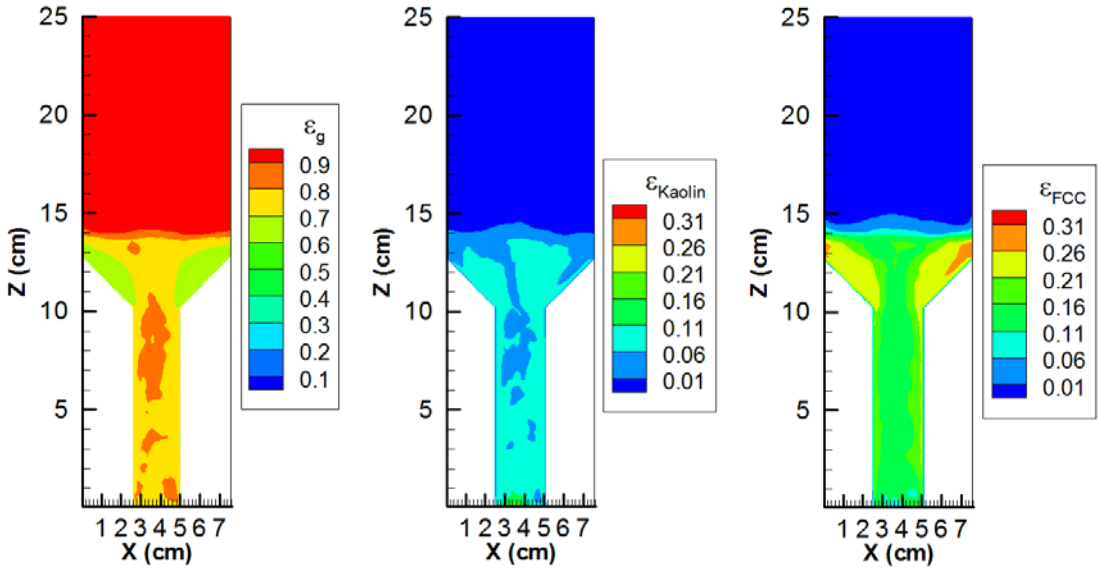

(a) (b) (c)

Fig. 3.5. Time and spatial-averaged contours of volume fractions for (a) gas, (b) Kaolin, and (c) FCC.

In analyzing gas-solid reactions, it was important to select a conceptual model that reasonably represents the physics of the problem. An unreacted core shrinking model was chosen, which is widely used in fluidized bed applications. The model choice is based on the assumption that heterogeneous surface reactions will occur in the system, and is valid when the chemical reaction is very fast and diffusion is the rate-determining step. At first, the reaction takes place at the outside surface of the particle, but as the reaction proceeds, the surface of the reaction will move into the interior of the solid. During the process, the reacting surface moves inward forming an unreacted core that shrinks with time, but the external radius of the particle still remains the same. In order for the gas reactants to reach the surface of the unreacted core, it must move through various layers in series: the gas film around the particle surface, the porous ash layer and then the reaction surface at the core.

Simulation of a chemically reacting flow that involves non-equilibrium chemistry requires careful computational modeling of the most important chemical kinetics. Modeling the full chemistry set is computationally expensive because it requires solving a large set of stiff ordinary differential equations. A commonly employed strategy is to use a fractional step approach to separate the chemical reactions from the rest of the transport processes (e.g., convection and molecular diffusion). The fractional step approach facilitates programming so that the reaction computations are isolated and efficiently solved in a “reaction module”. CHEMKIN is used for the computation of thermochemical properties and the reaction rates for the gaseous mixtures. There are two methods that can be used for the integration of the reaction step: the VODE stiff solver and in situ adaptive tabulation (ISAT). The VODE solver integrates the reaction equations with maximum efficiency and introduces no extra numerical error. ISAT employs an adaptive algorithm to dynamically tabulate the access region in a multi-dimensional composition space, which in certain cases gives computational speed-up by a factor of 50 or more, but can also introduce interpolation errors that must be carefully controlled. We performed tests to compare the performance of the ISAT and VODE methods. As the model

problem, we used the pair-wise mixing stirred reactor model for coal gasification for the tests. The tests were successful and are not shown here for brevity.

For homogeneous gas-phase chemical reactions, arbitrary chemical reaction mechanisms are incorporated into mass and energy conservation principles and the rate of reactions are expressed as the law of mass-action formulation. In contrast, there is considerably less standardization when considering surface chemical reactions. A number of classical rate expressions commonly used to characterize heterogeneous reactions include: Langmuir adsorption isotherm, Langmuir-Hinshelwood kinetics, and competitive adsorption, to name a few. An alternative approach to implement surface reactions is the SURFACE CHEMKIN, which is developed to provide a general framework for describing the heterogeneous chemical reactions. Surface processes are written as balanced chemical reactions governed by the law of mass-action kinetics. The main advantage of this formalism is that many of the classical surface rate expressions can be expressed in SURFACE CHEMKIN form and thus, can easily be implemented with minimum effort.

The implementation of SURFACE CHEMKIN in our CFD code is somewhat straight forward via the interface we have previously developed. A commonly employed strategy in CFD is to use a reaction fractional step to separate the chemical reactions from the rest of the transport processes such as convection and molecular diffusion. This enables the code to isolate the reaction computations into a separate and independent reaction module (or subroutine), and by using a unified interface to the rest of the program this reaction module allows implementations of various kinetics computation methodologies for maximum efficiency. Our previously developed interface is extended in this project to include surface kinetics. The module incorporates various libraries. CHEMKIN is used for computation of thermochemical properties and reaction rates for gaseous mixtures and the SURFACE CHEMKIN package is included to accounts for surface reaction rates. By using a unified interface, this reaction module allows easy implementations of various chemical kinetics representations. In this period, our previously developed interface is extended to include SURFACE CHEMKIN. This implementation provides several advantages such as: efficient handling of large reaction mechanisms, generalized framework with simple and standard inputs, minimization of common mistakes, common platform for distributing new products and possibility of using efficient representation of complex chemistry. The module incorporates various libraries. CHEMKIN is used for computation of thermochemical properties and reaction rates for gaseous mixtures and the SURFACE CHEMKIN package is included to accounts for surface reaction rates. The SURFACE CHEMKIN has its own interpreter (similar to CHEMKIN) which reads the input file "surf.inp", which is provided by the user and includes the chemical mechanism rate coefficients.

We initiated a study to design the two-stage fluidiziation unit. The process allowed for changing the diameters of the first stage and second stage sections as well as the angle of the second stage expansion. The key in this process also involves the prediction of the reactions. The chemically reacting systems can be classified into two general classes: homogeneous and heterogeneous systems. In homogeneous systems, reaction occurs among products and reactants that are in the same phase. In contrast, heterogeneous systems involve chemical reactions in which chemical species transform from one phase to another. As a result, in these systems characterization of species is much more involved because the species can reside in the gas phase, within the material (bulk phase) or on the surface phase (the interface between gas and bulk phases). The species that are adsorbed on the surface are considered to occupy one or more surface “sites”. The chemical reaction can also occur with each phase or on the surface (sites). The rate of deposition of species on the surface is governed by both chemical kinetics and the diffusion rate from the fluid to the surface. Surface reactions create sources or sinks of chemical species in the bulk or gas phase and determine the rate of deposition of surface species.

An analytical method, that we call the MASS method, was developed to predict fluidization characteristics by considering the portion of the bed material that fluidizes. Figure 3.6 shows the pressure drop curves for the experiments (Task 2) MFIX data, and the MASS method. The MASS method accurately predicts both the pressure drop and the minimum fluidization velocity for the binary system therefore, it is expected that the method can also predict segregation. The unfluidized mass fraction trends with increasing inlet gas velocity as predicted by the MASS method are shown in Figure 3.7. The curves for Kaolin and FCC show a high propensity for segregation, illustrated by the large magnitude of the initial slopes of the curves. The case suggests that the larger, more slowly fluidizing Kaolin particle will dominate the lower region of the reactor, while the smaller, more quickly fluidizing FCC particle will dominate the upper region of the reactor.

The MASS method and MFIX simulations are used to demonstrate the X_{FCC} distribution with height in Figure 3.8 for superficial inlet gas velocities of U_g = 1.0, 4.3, 5.7, and 6.5 cm/s. Heavy segregation can be seen in Figure 3.8, where at U_g = 1 cm/s, the unfluidized bed is composed of 11% FCC, while the fluidized region is 60% FCC. This results in a predicted value of segregation of $|X_{FCC,fluid} - X_{FCC,unfluid}|$ = 0.49. At higher inlet gas velocities, heavy segregation becomes more obvious when the unfluidized portion of the bed contains 0% FCC (only Kaolin is present). There is good agreement between the MFIX and MASS method for the prediction of segregation in the binary system. We show that the binary mixture of Kaolin and FCC has a high propensity to segregate. Therefore it is expected that under the correct flow conditions, the system should demonstrate considerable segregation above the minimum fluidization velocity. MFIX simulations will be used to help visualize how the materials segregate.

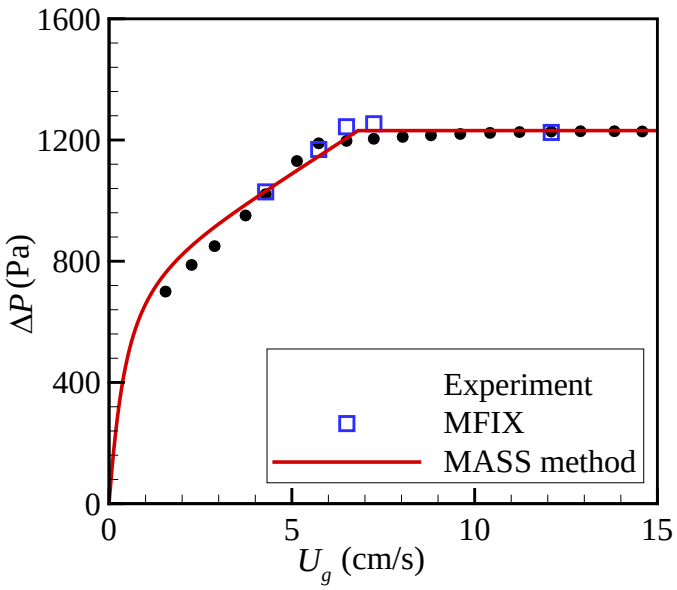

Figure 3.6. Binary system of FCC and Kaolin pressure drop versus inlet gas velocity

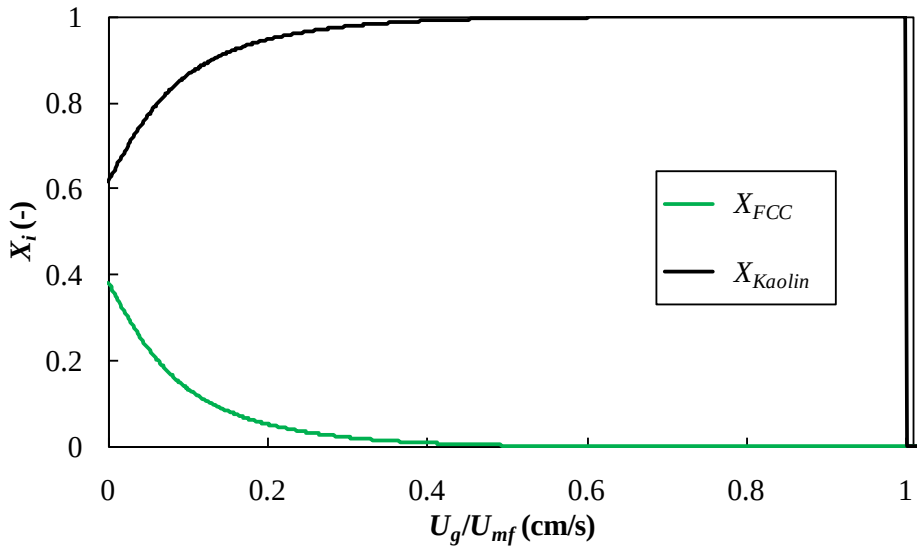

Figure 3.7. Binary system of FCC and Kaolin unfluidized bed mass fractions versus dimensionless inlet velocity.

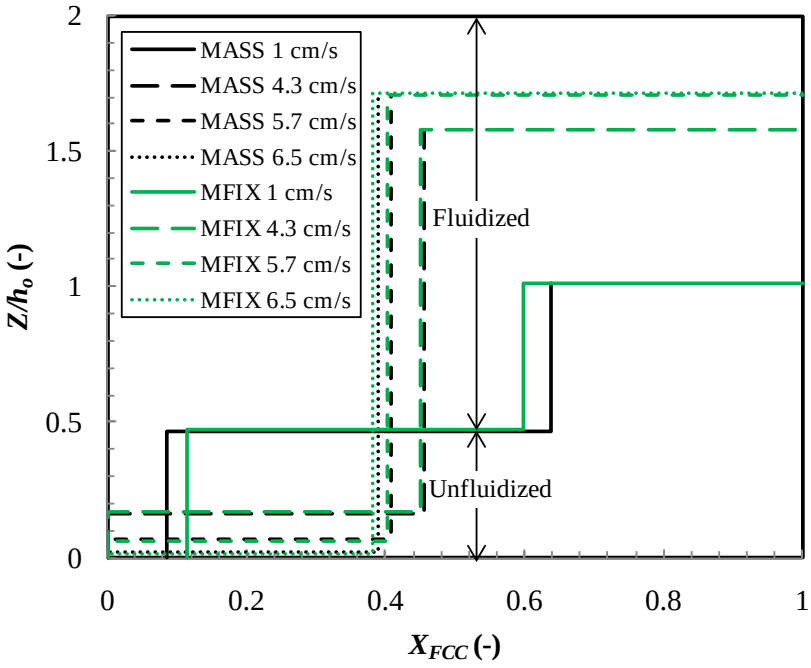

Figure 3.8. FCC mass fraction distributions versus dimensionless vertical height for various inlet gas velocities comparing MFIX simulation and MASS method.

Figures 3.9–3.10 present volume fraction contours for (a) gas, (b) Kaolin and (c) FCC based on MFIX simulations for U_g = 7.2 and 12.1 cm/s, respectively. The inlet gas velocity of 7.2 cm/s, is higher than the system minimum fluidization velocity of 6.8 cm/s and within the bubbling flow regime. Figure 3.9a shows small gas bubbles (small "pockets" of red) that are indicative of a mildly bubbling bed. The volume fractions reveal that the region up to 4 cm is dominated by the larger Kaolin particles (b), while the region from 4 cm to 17 cm is dominated by the smaller FCC particles (c). It is interesting to note that the lower region and the upper region exhibit different flow characteristics. The upper region is clearly a bubbling flow regime, shown as the blue bubbles in Figure 3.9(c), and the lower region demonstrates no bubbling behavior.

Figure 3.10 is data for U_g = 12.1 cm/s, which is a more rapidly bubbling bed. A small amount of segregation is observable with Kaolin slightly more prevalent in the lower region up to 9 cm (b), and FCC slightly more prevalent in the upper region from 9 cm to 19 cm (c). However, the extent of segregation is greatly reduced and the Kaolin and FCC particles are fluidizing to create a relatively well-mixed bed.

Previous research has suggested that the amount of segregation after fluidization is determined by the flow regime of the mixture. However, from the findings presented here it seems likely that differing component flow regimes promote high segregation while similar component flow regimes promote less segregation. At an inlet gas velocity of 7.2 cm/s the FCC is well above its individual component minimum fluidization velocity of 0.2 cm/s and exhibits a bubbling flow, while the Kaolin is just slightly above its individual component minimum fluidization velocity of 6.8 cm/s and experiences no bubbling behavior. The difference between the FCC and Kaolin flow regimes promotes heavy segregation between the components. At an inlet gas velocity of 12.1 cm/s the FCC exhibits a heavy bubbling flow and Kaolin exhibits a bubbling flow. The similarity between the FCC and Kaolin flow regimes promotes mixing between the components. Similarly, the heavy segregation experienced at inlet gas velocities bellow the systems minimum fluidization velocity is the result of dissimilar component flow regimes. An example is at U_g = 4.3 cm/s, which is below the minimum fluidization velocity of Kaolin, $U_{mf,Kaolin}$ = 6.8 cm/s, and above that of FCC, $U_{mf,FCC}$ = 0.2 cm/s. Therefore the FCC is in the fluidized flow regime and the Kaolin is not, resulting in heavy segregation between the components in the bed as shown in Figure 3.9.

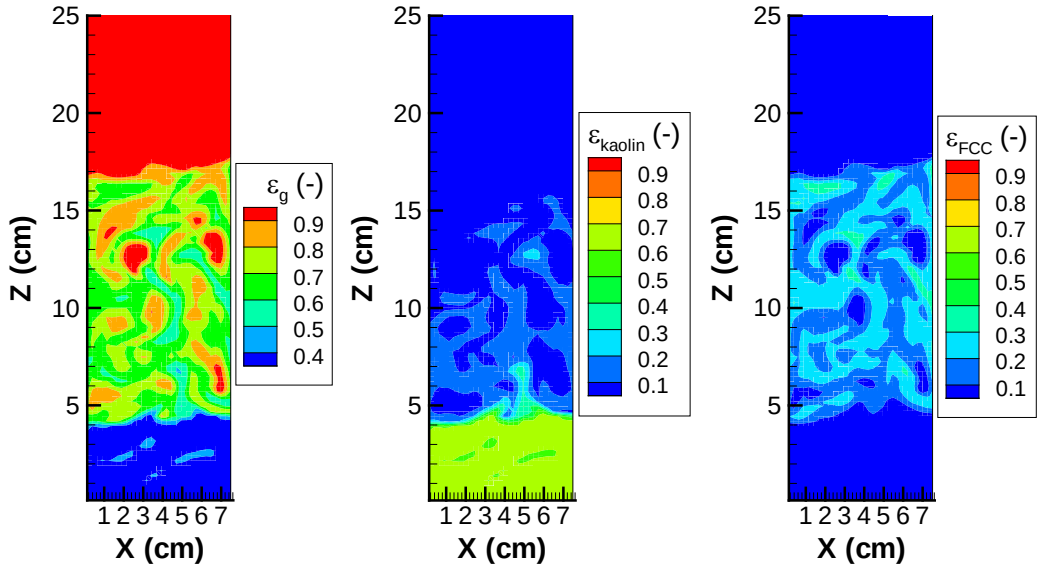

(a) Gas (b) Kaolin (c) FCC

Figure 3.9. Binary system instantaneous volume fraction MFIX simulations for inlet velocity of 7.2 cm/s (a) gas, (b) Kaolin, and (c) FCC

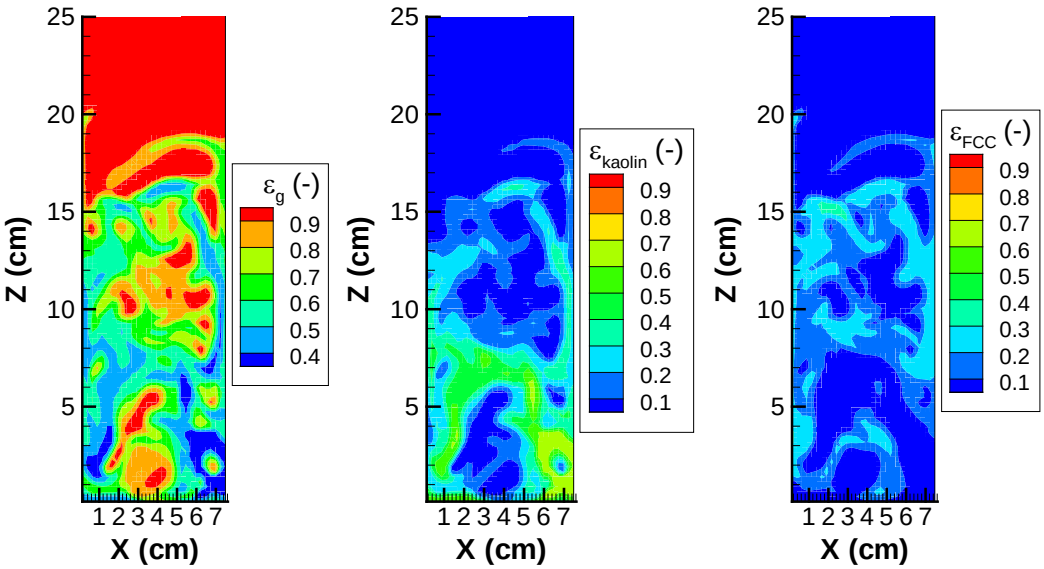

(a) Gas (b) Kaolin (c) FCC

Figure 3.10 Binary system instantaneous volume fraction MFIX simulations for inlet velocity of 12.1 cm/s (a) gas, (b) Kaolin, and (c) FCC

Pressure fluctuation analysis was used to study the features of the fluidized bed, which can be related to the motion of the gas bubbles forming and rising during the process. Analysis of the pressure fluctuations can be grouped according to their domain in time-, frequency- and space-domain analysis. For these studies, time- and frequency-domain analyses have been used to characterize the fluidization regimes. In the time-domain, plotting a sequence of pressure data points is the simplest method; however, another method is the standard deviation of pressure signals. Power spectral density (PSD) is a frequency-domain analysis to find dominant frequencies in the pressure data and relate them to physical phenomena.

To provide background, standard deviation of pressure fluctuations has been used to identify flow fluidization regimes where a gas velocity is associated with each regime transition. In contrast, the frequency-domain analysis is performed using a Fourier transform. The objective is to determine dominant frequencies in the time-series. Details pertaining to the equations can be found in the literature). A transfer function can be used to present the PSD as a Bode plot. What is unique about the fluidized bed system is that it is a second-order dynamical system that has a characteristic -40 dB/decade roll-off. The Bode plot is used to determine if the system is underdamped or overdamped.

Pressure data is presented in Figs. 3.11-3.13 using three analysis techniques where distinct features will be identified for each fluidization regime. In part (a) of each figure, pressure drop for a 25 s time period is shown to demonstrate how the pressure drop fluctuates with time. Pressure drop for all the cases have been shifted to zero to help quantify the fluctuation around the mean value. For part (b) of the figures, the PSD is shown for data collected over 195 s and the Bode plots are shown in part (c). The pressure drop has a minimum and maximum of approximately +/- 1 kPa for the bubbling fluidization regime (Fig. 3.11 (a)), but for other fluidization regimes, (Figs. 3.12 (a), 3.13 (a)) the pressure drop fluctuations are more pronounced.

PSD and Bode plots for the bubbling regime (Fig. 3.11(b) and (c)) show a series of peaks, which can be described as a broad peak between 2 and 4 Hz, with a maximum at f_B =2.6 Hz, where the subscript B denotes the bubbling fluidization regime. A similar trend for the PSD was obtained from the experiments of Johnson et al. [56] for a fluidized bed in the bubbling regime. The slugging fluidization regime PSD and Bode plots (Fig. 3.12(b) and (c)) show two broad peaks at lower frequencies over a range of 1.5 to 5 Hz, with a peak $f_{S;1}$ = 2 Hz and another peak at $f_{S;2}$ = 3:5 Hz, where the subscript S denotes the slugging fluidization regime. However, the magnitudes of these peaks are lower than the peak in the bubbling regime (Fig. 3.11). These distinctive broad peaks correspond to previous observations of two peaks at low frequencies, which were identified as characteristics of the slugging regime spectrum. For fluidized beds in the turbulent fluidization regime, one peak at approximately $f_{T;1}$ = 2 Hz and a broader peak at $f_{T;2}$ = 4:5 Hz are identified in the PSD and Bode plot (Fig. 3.13(b) and (c)). With increasing inlet velocity, the frequencies corresponding to the higher peaks will decrease. For these cases, the peak at lower frequency has a greater magnitude. The existence of two peaks in the spectrum of a turbulent fluidized bed have also been reported.

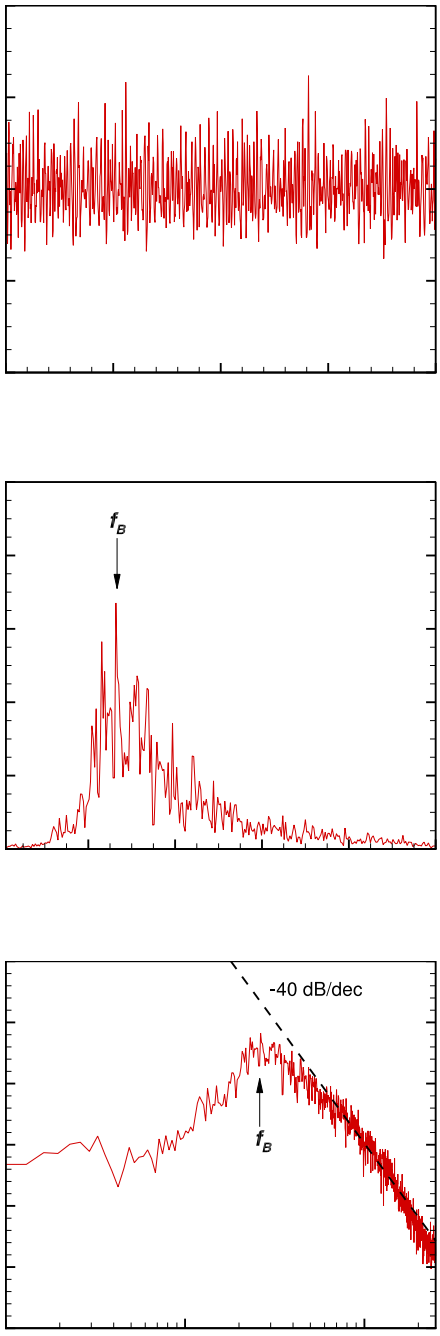

Figure 3.11 Pressure drop fluctuation (a) with time, (b) as a PSD analysis, and (c) as a Bode plot for the bubbling fluidized regime ($4U_{mf}$).

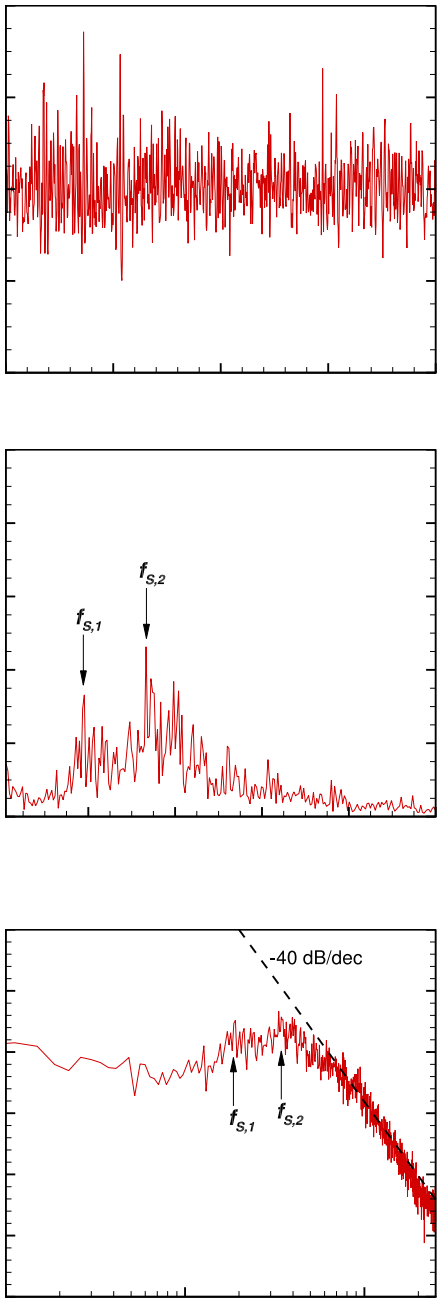

Figure 3.11 Pressure drop fluctuation (a) with time, (b) as a PSD analysis, and (c) as a Bode plot for the slugging fluidized regime ($6U_{mf}$).

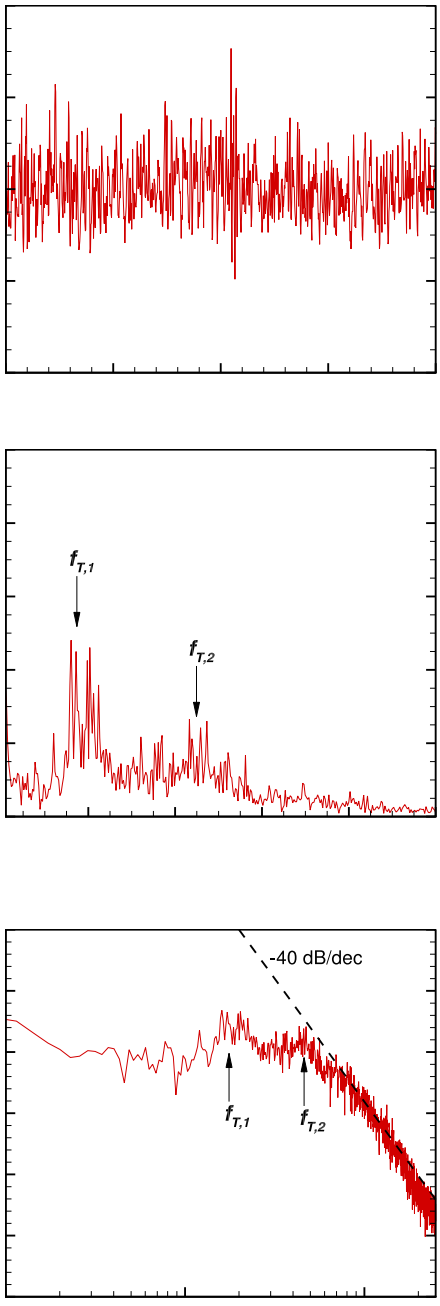

Figure 3.11 Pressure drop fluctuation (a) with time, (b) as a PSD analysis, and (c) as a Bode plot for the turbulent fluidized regime ($8U_{mf}$).

Task number: D. Modeling of the kinetics of product formation (Klein)

1. **Planned Activities**:

    D.1.1 The selection of biomass feed and product lumps
    D.1.2 The automated generation of kinetics model equations
    D.1.3 Estimating the kinetic parameters
    D.1.4 Construction of an engineering design package
    D.2.1 The selection of biomass feed molecules
    D.2.2 The automated generation of molecular model equations
    D.2.3 Estimating the molecular kinetic parameters
    D.2.4 Construction of a molecule-based engineering design package

This final report is provided upon the conclusion of the Sub-Contract between Virginia Polytechnic Institute and State University (Virginia Tech) and the University of Delaware for the DOE

Stated Objective:

The detailed analysis of the products of reaction from both model and real feedstocks will allow understanding of the major pathways involved, and will allow identification of bottlenecks, and their elimination.

Selection of Biomass Feed and Product Lumps

The selection of the feed and product lumps is guided by the nature of the predictions sought by the kinetics model. Coarse-lumped models are sufficient when only global predictions, such as weight loss and total gas, liquid, tar and char yields are desired. Finer-lumped models, including molecule-based models, are required the model is to provide more detailed information, such as the properties of the coarse lumps or the design of catalyst and operating conditions for optimal processing. This quarter's work addresses both scenarios.

The coarse-grained lumps are total gas, liquid, tar and char fractions. The gas lump includes CH4, CO2, CO, H2, C2H6 and C2H4. The liquid fraction includes both chemical and physical (i.e., associated) H2O, as well as MeOH, Acetone, ethylene glycol, acetol, methylglyoxal, acetaldehydes, and small carboxylic acids. The tar fraction is a collection of oxygenates, including variously substituted phenolics and a collection of ethers and esters. Multi-ring aromatics can form as well. The char fraction is defined, operationally, as the non-volatile residue.

The literature provides ample guidance on the reaction networks that connect these feed and product lumps into a reaction network. Many practical models contain three feed lumps, one for each of the cellulose, hemi-cellulose and lignin components of biomass. These feed lumps react to the product lumps noted above via reaction networks to be described in the next quarterly report. In brief, however, the network includes parallel and serial reactions including both starting and activated feed species.

The finer-grained lumps represent the molecules in the gas and liquid fractions noted above and expand the tar fraction into a molecular representation. The cellulosic tars include cellobiosan, glucose, fructose, and levoglucosan, whereas the lignin-derived tars include at least 30 different para-substituted methoxy-phenols that can be linked to the coniferyl, sinapyl and coumaryl alcohol lignin monomers. The lignin molecules are represented as the juxtaposition of two attributes: the first attribute describes the structure of the para substituent (noted above) and the second attribute describes the structure of the methoxyphenol moiety. These attributes are shown in Table 1 for a "Freudenberg" native lignin. A similar grid exists for various lignin preparations, including those from pulping processes.

Table 1. Initial lignin (Freudenberg) structure in terms of methoxyphenol (MP) and Propanoid Side Chain (PC) attributes[1]

MP	PC		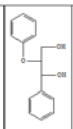	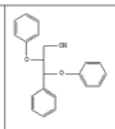	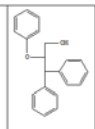	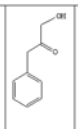	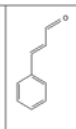	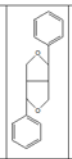	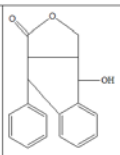	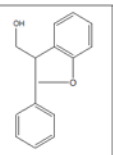	Sum
Normalized Distribution			0.33	0.11	0.11	0.11	0.06	0.11	0.11	0.06	1.00
 CONIFERYL	Free	0.28	1.67	0.56	0.56	0.56	0.28	0.56	0.56	0.28	5.00
	Etherified	0.56	3.33	1.11	1.11	1.11	0.56	1.11	1.11	0.56	10.00
 COUMARYL	Free	0.06	0.33	0.11	0.11	0.11	0.06	0.11	0.11	0.06	1.00
	Etherified	0.06	0.33	0.11	0.11	0.11	0.06	0.11	0.11	0.06	1.00
 SINAPYL	Free	0.00	0.00	0.00	0.00	0.00	0.00	0.00	0.00	0.00	0.00
	Etherified	0.06	0.33	0.11	0.11	0.11	0.06	0.11	0.11	0.06	1.00
	Sum	1.00	6.00	2.00	2.00	2.00	1.00	2.00	2.00	1.00	18.00

References

[1] Zhen Hou, Craig.A. Bennett, Michael T. Klein, Preetinder S. Virk "Approaches and Software Tools for Modeling Lignin Pyrolysis" *Energy & Fuels* **2010** *24* (1), 58-67

The Automated Generation of Kinetics Model Equations

Work during the third quarter led to the successful development of a software tool for the automated generation of kinetics models for biomass conversion and product upgrading. This advance removes the need to create these large models, i.e., models containing thousands of species and therefore associated reactions and reaction parameters, by hand, which is not only tedious and time consuming but also prone to error.

This software tool exploited the recognition that the chemical reactions of biomass conversion can be described by various quantitative combinations of free radical and acid- and metal-catalyzed chemistries. Combining these three "fundamental" reactions at both the pathways and

mechanistic levels has led to the development of INGen (Interactive Network Generator), the automated generator of kinetics model equations. A user-friendly interface eliminates the need for the user to have programming skills to incorporate different process chemistries for the creation of the biomass kinetic model. INGen's front end provides an easy to use interface, written into Excel, which allows the user to select biomass feed and reaction families and to set limits on carbon number, number of branches, species DelPlot rank, and number of reactions.

Within the working code of INGen, individual molecules are represented as adjacency lists that specify all of the connected nodes (atoms) to which each node (atom) is connected along with its edge value (bond order). A large library of pre-constructed biomass (lignocellulosic) species' adjacency lists are included with INGen, and new adjacency lists can be easily created by creating the species with CambridgeSoft's ChemDraw package and converting it using INGen.

During model generation, a chemical reaction is "written" when one species' graph is converted into a different graph. This conversion takes place when bonds are broken and formed between atoms. By identifying the active atomic sites of the reaction in a standard order, a universal reaction operator can be applied to those sites. A reaction is defined by three properties: the site neighborhood, the reaction site, and the reaction operator. The site neighborhood provides mechanistic information within a pathways level reaction. The reaction site itself defines which atoms will take part in the reaction (and the order in which they will be acted upon). The reaction operator defines how to affect the bonds of the site atoms.

INGen now includes the mechanistic reactions for free-radical and acid- and metal-catalyzed chemistries listed in Table 2 as well as the multistep pathways level reactions listed in Table 3.

Table 2. Mechanism-Level Reaction Families

Free Radical	Acid	Metal
Bond fission	Ionic Isomerization	Hydrogenation
Radical hydrogen Abstraction	Ionic Hydride Shift	Dehydorgenation
Radical Beta-Scission	Ionic Methyl Shift	Hydrogenolysis
Radical Addition	Ionic Beta-Scission	
Radial Termination	Ionic Hydrogen Abstraction	
	Ionic Protonation	
	Ionic Deprotonation	
	Ionic Ring Closure	
	Ionic Ring Expansion	
	Ionic Addition	

Table 3. Pathways-Level Reaction Families

Isomerization	Denitrogenation
Cyclization	Ring Saturation
Hydrogenolysis	Dealkylation
Cracking	Side Chain Cracking
Double Bond Shift	Ring Closure
Hydrogenation	Ring Opening
Hydrodesulfurization	Ring Isomerization

The resultant reaction network is written in a KME (Kinetic Model Editor) compatible form that can then be analyzed, as follows. Each species is listed along with its rank, molecular weight,

carbon number, hydrogen count, type, and IUPAC name. In addition, a ChemDraw graphic can be automatically created for each species simply by clicking on it.

INGen was used to create a hydroprocessing network where very good species identification and analysis was performed for both the feed and product streams, thereby defining the model's desired footprint.

A series of model building experiments were run in order to produce the desired reaction network. Figure 1 illustrates a dramatic decrease in the number of reactions and species as rank limitations are placed on the network generation. Each run was completed and analyzed within minutes, thereby demonstrating the real power of INGen.

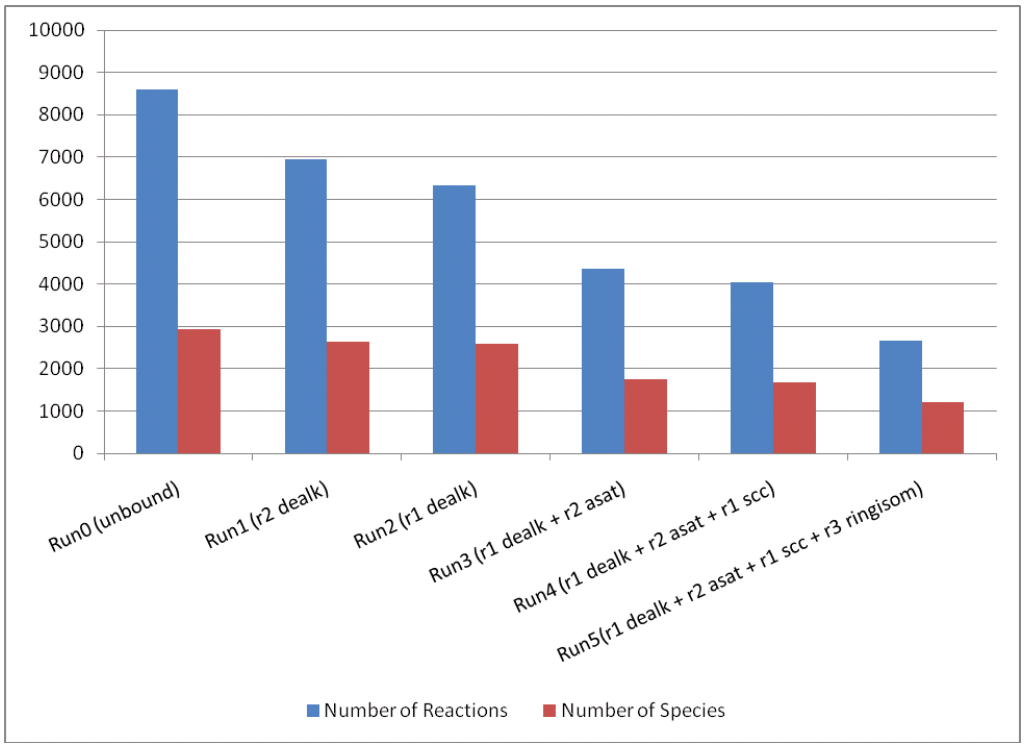

Figure 1. Results of Rank Limitations for a Hydroprocessing Network

Estimating the Kinetic Parameters

Work during the fourth quarter focused on generalizing reaction functions and enhancing olefin and double-bond chemistries, oxygen chemistries, and cellulose pyrolysis pathways in INGen, in addition to obtaining estimates of kinetic parameters for use within INGen. It is necessary to expand the reaction functions within INGen to incorporate non-bonded sites, as well as to further develop the double-bond (olefin) pathways, to include more complex chemistries. The chemistry of the creation and reaction of olefins was reviewed to include pathways reactions with olefinic intermediates.

In an effort to broaden the feedstock capability of INGen, reaction pathways beginning with cellulose were studied. Cellulose pyrolysis primarily follows two competing pathways: one forming levoglucosan, the other forming glycolaldehyde. Pathway selectivity is weakly influenced by temperature and strongly influenced by salt and metal ion presence, though these

effects are not well understood. It is believed that cellulose dehydration is the initiation step for both pathways. Cellulose decomposition at low to moderate heating rates is dominated by a single rate-limiting step, which is well modeled by a single-step, high activation energy, first-order model. [2] It is necessary to understand the details of the reaction pathways in order to construct a representative reaction matrix for use in INGen.

The dehydration of cellulose was examined from a mechanistic point of view in order to establish the reaction site neighborhoods that must be present for the dehydration to occur. Cellulose dehydration is believed to occur in the presence of an acid catalyst by the protonation of a terminal OH group, forming an OH_2^+ leaving group, allowing the O linking cellulose monomers to attack the now partially charged carbon originally attached to the OH_2^+ leaving group, forming (n + 2) dehydrated intermediate molecules and water. The dehydrated intermediate then undergoes either an isomerization reaction to levoglucosan (as depicted in Fig. 9 [7]), or reacts to form glycolaldehyde. [7] With the incorporation of these dehydration pathways and oxygenated biomolecules, INGen will have the ability to take a cellulose feedstock and model its pyrolysis to final products, as it is currently capable with other feedstocks.

By looking from both mechanistic and ARM-pathways points of view, it is apparent that some reactions cannot be modeled by the ARM (Attribute Reaction Model) approach, namely ring-altering reactions. In these cases, the specific mechanisms must be analyzed to formulate an appropriate reaction matrix. Similarities between cellulose (or hemicellulose) and lignin pyrolysis exist in that they both involve dual site chemistries, although the present research suggests that attribute reaction modeling will not be an appropriate method for incorporating cellulose into INGen unless a third layer of complexity is introduced via side chain chemistry.

INGen was updated such that bond chains were no longer necessary for the specification of a reaction site. Instead, larger reaction site neighborhoods that allow reactions to take place are identified. These determine the reaction mechanism in increasingly large and complex species, such as cellulose. Within the reaction site neighborhood, the active atoms that break or form bonds during the reaction comprise the reaction site.

Corresponding kinetic parameters are necessary for application of these newly added reaction mechanisms and pathways. Kinetic parameter estimates were obtained in the literature for the two primary cellulose pyrolysis pathways noted above. Mamleev and others [6] summarize the kinetic parameters for “tar” (primarily levoglucosan) and “gas” pathways, calculated by three different research groups, in Table 4 [6], reproduced here:

Table 4 (Reproduced) [6]

	Bradbury et al. [4] in vacuum	Banyasz et al. [3] in N_2 at fast pyrolysis	Capart et al. [5] in N_2
E_{tar} (kJ/mol)	198	151.1	202.7
A_{tar} (s^{-1})	3.2×10^{14}	4.0×10^{10}	1.46×10^{15}
E_{gas} (kJ/mol)	153.2	195.9	255
A_{gas} (s^{-1})	1.3×10^{10}	1.0×10^{14}	2.66×10^{19}

With these cellulose pyrolysis kinetic parameter estimates, combined with those for other involved chemistries, INGen is prepared for kinetic parameter tuning using experimental data.

References

[2] Antal MJJ, Varhegyi G. "Cellulose Pyrolysis Kinetics: The Current State of Knowledge". Industrial & Engineering Chemistry Research. 1995. 34 (3), 703-717.

[3] Banyasz JL, Li S, Lyons-Hart J, Shafer KH. Fuel 80 (2001) 1757–1763.

[4] Bradbury AGW, Sakai Y, Shafizadeh F. J. Appl. Polym. Sci. 23 (1979) 3271–3280.

[5] Capart R, Khezami L, Burnham AK. Thermochim. Acta 417 (2004) 79–89.

[6] Mamleev V, Bourbigot S, Yvon J. "Kinetic analysis of the thermal decomposition of cellulose: The change of the rate limitation". Journal of Analytical and Applied Pyrolysis. 2007. 80 (1), 141-150.

[7] Wershaw RL. "Evaluation of conceptual models of natural organic matter (humus) from a consideration of the chemical and biochemical processes of humification". Reston, Va.: U.S. Dept. of the Interior, U.S. Geological Survey; Denver, CO : U.S. Geological Survey, Information Services [distributor], 2004.

Construction of an Engineering Package

Work during the fifth quarter focused on identifying the reaction families and pathways involved in cellulose pyrolysis. Detailed knowledge of site neighborhoods, associated mechanisms, and overall understanding of pathways-level reactions are necessary for inclusion in INGen. Expanding INGen to include cellulose chemistries will allow for the inclusion of cellulose as a pyrolysis feedstock in models, making INGen a more comprehensive biomass pyrolysis Interactive Network Generator. Cellulose depolymerization and subsequent oxygen chemistries are the two areas that are being investigated.

Macromolecular cellulose, with chain lengths ranging from about 7000 to 15000 monomers, depolymerize via two pathways: via levoglucosan [8,9,10,11,12,13,14] or glycolaldehyde [9,10,11,13]. The kinetic parameter estimates provided in the Fourth Quarterly Report for "tar" and "gas" pathways refer to these, respectively. The levoglucosan pathway is both better understood and more dominant. As a result, the pathway can be modeled fully, including both the initial depolymerization step and the subsequent reactions.

The depolymerization of cellulose to levoglucosan follows an unzipping mechanism that can be modeled using INGen via an ARM (Attribute Reaction Model) pathway such that individual levoglucosan molecules break from the ends of the unbranched cellulose chains until the depolymerization is complete. The levoglucosan molecules then undergo dehydration to methylglyoxal, followed by hydrogenation to acetol, then to propylene glycol, finally forming isopropanol via hydrogenolysis. [14] The hydrogenation and hydrogenolysis reaction families

are readily generalized for use in INGen as reaction matrices. The depolymerization and dehydration steps are specific to the cellulose-levoglucosan pathway and will be included in INGen during expansion to cellulose pyrolysis.

The site neighborhood for depolymerization of cellulose to levoglucosan has been identified as an oxygenated ring with a hydroxymethyl group beta to an ether linkage. For the oxygenated reaction families of hydrogenation and hydrogenolysis, simple site neighborhoods are identified. Hydrogenation can occur wherever a ketone group exists, with one hydrogen atom adding to the oxygen and the other adding to the associated carbon, resulting in an alcohol group. Hydrogenolysis can occur wherever a carbon-oxygen single bond exists, cleaving the bond by addition of hydrogen.

With these added cellulose pathways and oxygenated reaction families, INGen will be capable of including cellulose as a pyrolysis feedstock for network generation in addition to its current capabilities for lignin pyrolysis. The kinetic network will then be input to KME, thereby constructing the model equations. Tuning of the pre-exponential A factor and the activation energy parameters based on observed data can then begin using the kinetic parameter estimates obtained last quarter.

References

[8] Antal MJ, Friedman HL, Rogers FE. “Kinetics of Cellulose Pyrolysis in Nitrogen and Steam”. *Combustion Science and Technology*. 1980. 21, 141-152.

[9] Antal MJ, Varhegyi G. “Cellulose Pyrolysis Kinetics: The Current State of Knowledge”. *Industrial & Engineering Chemistry Research*. 1995. 34 (3), 703-717.

[10] Antal MJ, Varhegyi G. “Impact of Systematic Errors on the Determination of Cellulose Pyrolysis Kinetics”. *Energy & Fuels*. 1997. 11 (6), 1309-1310.

[11] Demirbas A. “Mechanisms of liquefaction and pyrolysis reactions of biomass”. *Energy Conversion and Management*. 2000. 41 (6), 633-646.

[12] Mamleev V, Bourbigot S, Yvon J. “Kinetic analysis of the thermal decomposition of cellulose: The change of the rate limitation”. *Journal of Analytical and Applied Pyrolysis*. 2007. 80 (1), 141-150.

[13] Varhegyi G, Jakab E, Antal MJ. “Is the Broido-Shafizadeh Model for Cellulose Pyrolysis True?” *Energy & Fuels*. 1994. 8, 1345-1352.

[14] Wershaw RL. “Evaluation of conceptual models of natural organic matter (humus) from a consideration of the chemical and biochemical processes of humification”. *Reston, Va.: U.S. Dept. of the Interior, U.S. Geological Survey*; Denver, CO : U.S. Geological Survey, Information Services [distributor], 2004.

Selection of Biomass Feed Molecules & Automated Generation of Molecular Model equations

Lumped biomass pyrolysis yield data was provided by the Agblevor group. The lumps defined in the data are organics, water, char, and gas. A reaction network for pyrolsis of each component of biomass into these lumps has been adapted from Di Blasi [15], where “biomass” and “activated biomass” refer to a single component (cellulose, hemicellulose, or lignin). The language used to describe the lumps in literature differs from that used by the Agblevor group, such that “tar” indicates “organics” and “refractory tars” are considered simply to be of the greater “tar” (“organics”) fraction.

$$\text{Biomass} \xrightarrow{k_0} \text{Activated Biomass}$$

$$\text{Activated Biomass} \xrightarrow{k_1} \text{Tar}$$

$$\text{Activated Biomass} \xrightarrow{k_2} \nu_C \text{Char} + (1-\nu_C)\text{Gas}$$

$$\text{Tar} \xrightarrow{k_3} \text{Gas}$$

$$\text{Tar} \xrightarrow{k_4} \nu_T \text{Refractory Tars} + (1-\nu_T)\text{Water}$$

A steady state assumption is made on the intermediate “Activated Biomass” lump, such that the reaction of “Biomass” to “Activated Biomass” is much faster than each of the other reactions. This is supported by the observation that logA for k_0 is much greater than logA for k_1 and k_2 from literature. We may then eliminate this immeasurable species from the model as a fleeting intermediate. The modified network is then written

$$\text{Feed} \xrightarrow{k_1} \text{Organics}$$

$$\text{Feed} \xrightarrow{k_2} \nu_C \text{Char} + (1-\nu_C)\text{Gas}$$

$$\text{Organics} \xrightarrow{k_3} \text{Gas}$$

$$\text{Organics} \xrightarrow{k_4} \nu_T \text{Organics} + (1-\nu_T)\text{Water}$$

The lumped reaction network was input in KME (Kinetic Model Editor) and the corresponding kinetic model equations were automatically generated. The kinetic parameters (pre-exponential factor and apparent first-order activation energy) were tuned using KME for each set of data. The tuned kinetic parameters are compared to corresponding values from literature where available. Values for the empirical stoichiometric coefficient ν_C are supplied by literature for each biomass component, while values for the stoichiometric coefficient ν_T are estimated from the experimental data provided by the Agblevor group. These values represent the relative formation of product lumps in the absence of balanced molecular-level reactions. Values for the kinetic parameters and ν_C are adapted from Di Blasi [15] in Table 5 below.

Table 5. Values for lumped kinetic parameters and char stoichiometric coefficient ν_c, Di Blasi [15]

Feedstock	k_0		k_1		k_2		ν_c
	logA	E*	logA	E*	logA	E*	
Cellulose	19.4	57.9	14.5	46.9	10.1	35.9	0.35
Hemicellulose	16.3	44.6	15.9	48.3	11.4	34.8	0.60
Lignin	8.98	25.70	9.18	34.34	6.89	26.61	0.75

Pre-exponential factor A [=] s^{-1}, E* [=] kcal/mol.

The lumped kinetic parameters (pre-exponential factor and apparent first-order activation energy) and values of ν_T obtained from the data are given below in Table 6. Values for ν_c are taken from Table 5 [15] for the three corresponding biomass components. Values for ν_T are estimated by the ratio

ν_T = (Tar)/(Tar + Water)

Table 6. Values for lumped kinetic parameters and tar stoichiometric coefficient ν_T, Agblevor

Feedstock	Sample	k_1		k_2		k_3		k_4		ν_c	ν_T
		logA	E*	logA	E*	logA	E*	logA	E*		
Cellulose	MCC-sand	12.63	37.31	14.26	44.02	0.64	59.24	9.00	27.84	0.35	0.87
Cellulose	Na-MCC-sand	4.62	8.84	19.04	56.60	11.94	38.67	13.45	42.63	0.35	0.61
Cellulose	MCC-HZSM-5	17.21	14.43	12.69	1.28	15.11	48.58	17.45	56.14	0.35	0.49
Hemicellulose	Xylan-sand	15.63	42.52	9.75	23.22	13.39	21.43	9.77	9.11	0.60	0.23
Hemicellulose	Na-Xylan-sand	15.69	34.40	17.77	41.23	4.12	11.49	4.09	11.58	0.60	0.21
Hemicellulose	Xylan-HZSM-5	7.90	17.43	14.75	40.77	5.36	3.61	13.67	31.30	0.60	0.17
Lignin	KL-sand	8.40	6.98	19.62	43.03	10.79	35.70	8.52	25.73	0.75	0.20
Lignin	Na-KL-Sand	14.85	1.18	16.50	5.10	11.57	37.63	4.44	12.44	0.75	0.28
Lignin	KL-HZSM-5	7.38	20.70	9.18	25.63	4.75	14.90	4.71	12.51	0.75	0.09
Guaiacol	Guaiacol-sand	7.97	18.19	4.79	167.80	19.60	64.48	4.71	14.10	0.00	0.98
Guaiacol	Guaiacol-HZSM-5	19.82	46.72	18.72	44.09	12.28	81.59	1.90	4.55	0.00	0.95
Syringol	Syringol-sand	17.32	52.39	14.62	52.38	14.95	48.94	18.72	60.38	0.00	0.97
Syringol	Syringol-HZSM-5	17.69	46.09	11.93	28.12	7.39	155.57	16.42	52.51	0.00	0.86

Pre-exponential factor A [=] s^{-1}, E* [=] kcal/mol.

Comparing the experimental values in Table 6 to the literature values in Table 5 shows relative agreement, within acceptable ranges for lumped estimates. Larger discrepancies exist in samples with additives/catalysts, which decrease the apparent activation energies significantly in some cases. The predicted pyrolysis yields from KME were generally in good agreement with the observed yields provided by the Agblevor group, as shown in Table 7 below.

Table 7. Predicted versus observed pyrolysis yields, wt%.

Feedstock	Sample	Observed Pyrolysis Yields (wt%)				Predicted Pyrolysis Yields (wt%)			
		Organics	Char	Gas	Water	Organics	Char	Gas	Water
Cellulose	MCC-sand	62.0	10.1	18.5	9.5	62.0	10.0	18.6	9.5
Cellulose	Na-MCC-sand	18.8	18.2	51.0	11.8	18.2	17.4	50.2	10.5
Cellulose	MCC-HZSM-5	20.2	7.9	50.3	21.2	20.6	7.8	50.5	21.1
Hemicellulose	Xylan-sand	7.2	26.1	43.0	23.6	0.0	28.5	45.5	26.0
Hemicellulose	Na-Xylan-sand	4.6	30.8	46.8	17.8	4.6	30.8	46.6	18.1
Hemicellulose	Xylan-HZSM-5	4.8	21.5	49.6	24.2	0.0	23.1	51.2	25.8
Lignin	KL-sand	5.6	51.0	22.2	21.8	5.8	50.9	21.8	21.6
Lignin	Na-KL-Sand	5.4	55.8	24.8	14.0	5.4	55.7	25.0	13.9
Lignin	KL-HZSM-5	2.3	50.5	22.7	24.5	2.2	50.4	22.5	24.8
Guaiacol	Guaiacol-sand	65.7	0.0	32.9	1.4	65.8	0.0	32.8	1.4
Guaiacol	Guaiacol-HZSM-5	63.7	0.0	32.9	3.4	63.6	0.0	32.9	3.4
Syringol	Syringol-sand	64.9	0.0	33.1	2.0	64.9	0.0	33.1	2.0
Syringol	Syringol-HZSM-5	58.5	0.0	31.6	9.9	58.5	0.0	31.6	9.9

With this set of lumped kinetic parameters, we have demonstrated the ability of the KME software to determine kinetic parameters from a given set of cellulose (or other biomass component) pyrolysis data. The set of biomass feed molecules selected for study by the Agblevor group represent all three of the main components of biomass: cellulose, hemicellulose, and lignin. On a molecular level, our group will further represent lignin as the conjunction of Propanoid Side Chains with Methoxyphenolic substituents on an aromatic ring.

By breaking lignin into such independently reacting attributes, we have used KME to model lignin pyrolysis via an Attribute Reaction Model (ARM). Such a method was deemed inappropriate for the pyrolysis of cellulose and hemicelluloses, the pyrolysis of which will be modeled via an unzipping mechanism. The subsequent reactions are very straightforward and have been provided in the past for cellulose (and is currently being worked on for hemicelluloses). From all these molecule specific pyrolysis reactions, KME was able to automatically generate the set of molecular model equations, thereby building an un-tuned model.

References

[15] Di Blasi C. "Modeling chemical and physical processes of wood and biomass pyrolysis". Progress in Energy and Combustion Science. 2008. 34 (1), 47-90.

Estimation of Molecular Kinetic Parameters

Lumped biomass pyrolysis yield data was provided by the Agblevor group during the sixth quarter. The lumps defined in the data are organics, water, char, and gas. The reaction network for pyrolysis of each component of biomass into these lumps has been adapted from Di Blasi [16], reproduced here.

$$\text{Feed} \xrightarrow{k_1} \text{Organics}$$

$$\text{Feed} \xrightarrow{k_2} \nu_C \text{Char} + (1-\nu_C)\text{Gas}$$

$$\text{Organics} \xrightarrow{k_3} \text{Gas}$$

$$\text{Organics} \xrightarrow{k_4} \nu_T \text{Organics} + (1-\nu_T)\text{Water}$$

We were able to fit kinetic parameters (logA and E*) to this reaction network for the provided lumped pyrolysis yield data. The experimental data provided utilized model compounds for lignocelluosic biomass components (cellulose, hemicellulose, and lignin), pyrolyzed separately. This quarter, we simulated the lumped pyrolysis yields of synthesized biomass. Since biomass consists of a range of about 40-60% cellulose, 20-40% hemicellulose, and 10-25% lignin [17], three compositions were selected for comparative purposes: average composition of 50% cellulose, 30% hemicellulose, and 20% lignin; high cellulose composition of 60% cellulose, 30% hemicellulose, and 10% lignin; low cellulose composition of 40% cellulose, 30% hemicellulose, 30% lignin. The results of these simulations are summarized in Table 8.

Table 8. Simulated Biomass Pyrolysis Yields (wt%)

Set	Composition	Modeled				Weighted Observed			
		Organics	Char	Gas	Water	Organics	Char	Gas	Water
A	50%C + 30%H + 20%L	34.28	23.07	26.58	16.19	32.14	23.72	27.28	16.85
A	60%C + 30%H + 10%L	39.92	18.97	26.21	14.96	37.77	19.63	26.96	15.64
A	40%C + 30%H + 30%L	28.64	27.16	26.95	17.42	26.52	27.81	27.61	18.06
B	50%C + 30%H + 20%L	11.86	29.50	44.50	14.04	11.77	29.07	43.97	15.19
B	60%C + 30%H + 10%L	13.20	25.74	47.12	13.82	13.09	25.23	46.48	15.19
B	40%C + 30%H + 30%L	10.52	33.26	41.88	14.26	10.44	32.91	41.47	15.19
C	50%C + 30%H + 20%L	12.00	20.50	44.57	22.76	10.72	20.90	45.13	23.26
C	60%C + 30%H + 10%L	13.79	16.24	47.33	22.43	12.55	16.63	47.93	22.89
C	40%C + 30%H + 30%L	10.21	24.76	41.81	23.09	8.89	25.16	42.32	23.63

Comparison of the pyrolysis yields of these three compositions illustrates the favorability of lignocellulosic material with high cellulose content to obtain high organics yields. Thus, optimal lignicellulosic feedstocks may be selected for given applications based upon the proportions of cellulose, hemicellulose, and lignin. This discrimination is extremely useful as it can be used to eliminate materials as viable pyrolysis feedstocks for given applications without spending experimental resources.

As shown in Figure 2, the modeled simulated biomass pyrolysis yields are close, but not identical, to the observed yields (from the Agblevor data) weighted by the synthesized composition. There is an expected interaction between the pyrolysis of the biomass components because they produce similar lumps. Experiments utilizing a mixture of compounds as the pyrolysis feedstock will provide further insight into the causes of these interactions, which may then be exploited to obtain desired product compositions.

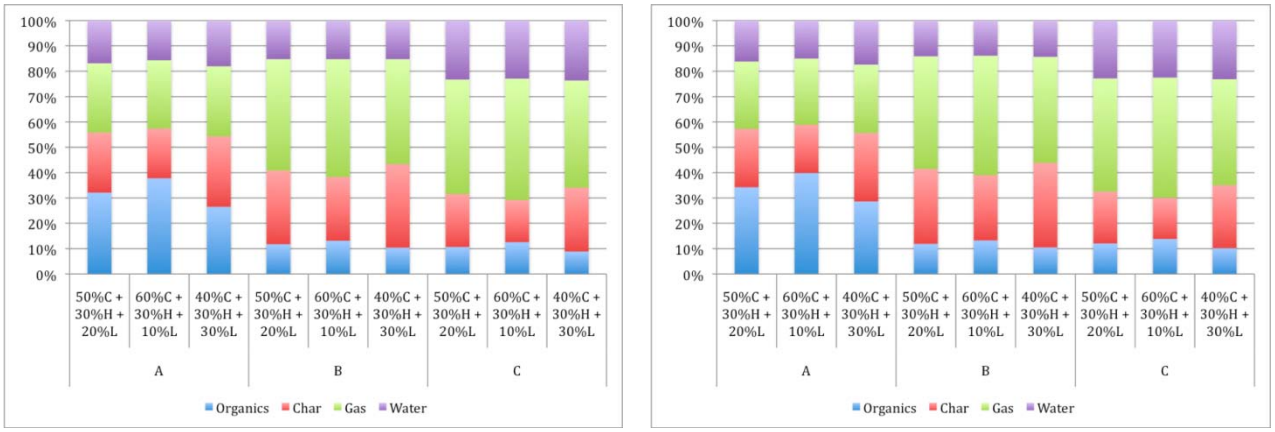

Figure 2. Simulated Biomass Pyrolysis Yields (wt%), Modeled versus Weighted Observed
a. Modeled **b.** Weighted Observed

Figure 3 gives yield comparisons between the three sets of data provided by the Agblevor group: Set A used sand as the fluidization medium; Set B was treated with sodium hydroxide and used sand as the fluidization medium; Set C used HZSM-5 as the fluidization medium. Set A maximizes organics yields, which is useful for the production of liquid fuels. Set B maximizes char production, which is undesired for fuel applications. Set C maximizes gas yields, which may be useful for the production of certain commodity gases or combined to form liquid fuels. The treatment method for lignocellulosic feedstocks may be selected based on these and other criteria to maximize the desired product fraction.

Figure 3. Simulated Biomass Pyrolysis Yields (wt%), by Set
a. Set A (sand-fluidized) **b.** Set B (NaOH-treated, sand-fluidized) **c.** Set C (HZSM-5-fluidized)

Simulating the pyrolysis of synthesized biomass provides some insight into the interactions between lignocellulosic components and treatment methods. Feedstocks and treatment methods may be selected to optimize production of a desired lump with these models. Added molecular detail will provide much deeper understanding of these interactions and facilitate well-informed feedstock and treatment selection.

References

[16] Di Blasi C. "Modeling chemical and physical processes of wood and biomass pyrolysis". *Progress in Energy and Combustion Science*. 2008. 34 (1), 47-90.

[17] Yang H, Yan R, Chen H, Zheng C, Lee DH, Liang DT. "In-depth investigation of biomass pyrolysis based on three major components: hemicellulose, cellulose and lignin". *Energy & Fuels*. 2006. 20 (1), 388-393.

Engineering Design

The work completed in the eighth quarter consisted of reinforcing the optimization of kinetic parameters in KME for the application of biomass pyrolysis. Focusing on a reaction network for cellulose, a model was developed and tuned to strengthen the overall biomass pyrolysis model produced by the KMT engineering design package. Parameter tuning for a literature-supported cellulose pyrolysis reaction network was performed to produce the most complete biomass pyrolysis model currently available.

The reaction network presented in Table 9 includes the major and minor pyrolysis pathways via levoglucosan and glycolaldehyde, respectively. Further reactions involving levoglucosan and its derivatives are reported in literature, as noted. Cellulose has an average degree of polymerization of near 1000, used as *x* for this example network. An additional pseudo-reaction to simulate char formation is also included.

Utilizing KME, the kinetic parameters (logA and E*) for each of these reactions was tuned. For the parameter tuning, a batch reactor of constant volume 1 L was selected, operating isothermally at 633 K, 1 atm, for 1 minute. The molar flow concentrations of the simulated feed, desired observed product, and modeled prediction for the product composition are listed in Table 10.

Table 9. Cellulose pyrolysis reaction network and kinetic parameters

Reaction	References	logA	E*[kcal/mol]
$cellulose_x \leftrightarrow x$ levoglucosan	[18], [19], [20], [24], [25], [26], [27]	13.2	45.6
$cellulose_x \leftrightarrow 3x$ glycolaldehyde	[19], [20], [25], [26]	8.48	34.4
levoglucosan $\leftrightarrow$ 2 methylglyoxal + H_2O	[24]	13.8	45.4
methylglyoxal + $H_2 \leftrightarrow$ acetol	[24]	6.00	34.3
acetol + $H_2 \leftrightarrow$ propylene glycol	[24]	8.09	11.0
propylene glycol + $H_2 \leftrightarrow$ isopropanol + H_2O	[24]	8.50	32.8
levoglucosan $\leftrightarrow$ 6 carbon + H_2O	-	11.1	66.3

Table 10. Cellulose feed and product composition

Species	Molar Concentration [mol/L]		
	Input	Observed	Predicted
cellulose	1.00E-01	-	8.31E-02
glycolaldehyde	-	-	6.78E+00
levoglucosan	-	-	9.58E+00
methylglyoxal	-	1.00E+01	1.00E+01
Water	-	-	5.02E+00
hydrogen	1.00E+00	-	9.99E-01
Acetol	-	-	7.77E-10
propylene glycol	-	-	3.09E-04
isopropanol	-	1.00E-05	7.14E-06
carbon	-	1.00E-10	3.01E-09

The solution to the objective function in KME tunes the parameters to appropriately fit the desired product composition. As discussed in previous reports, the same procedure is followed for true experimental data and corresponding microkinetic reaction network.

References

[18] Antal MJ, Friedman HL, Rogers FE. “Kinetics of Cellulose Pyrolysis in Nitrogen and Steam”. *Combustion Science and Technology*. 1980. 21, 141-152.

[19] Antal MJ, Varhegyi G. “Cellulose Pyrolysis Kinetics: The Current State of Knowledge”. *Industrial & Engineering Chemistry Research*. 1995. 34 (3), 703-717.

[20] Antal MJ, Varhegyi G. “Impact of Systematic Errors on the Determination of Cellulose Pyrolysis Kinetics”. *Energy & Fuels*. 1997. 11 (6), 1309-1310.

[21] Banyasz JL, Li S, Lyons-Hart J, Shafer KH. “Gas evolution and the mechanism of cellulose pyrolysis”. *Fuel*. 2001. 80 (12), 1757–1763.

[22] Bradbury AGW, Sakai Y, Shafizadeh F. “A kinetic model for pyrolysis of cellulose”. *Journal of Applied Polymer Science*. 1979. 23 (11), 3271–3280.

[23] Capart R, Khezami L, Burnham AK. “Assessment of various kinetic models for the pyrolysis of a microgranular cellulose”. *Thermochimica Acta*. 2004. 417 (1), 79–89.

[24] Demirbas A. “Mechanisms of liquefaction and pyrolysis reactions of biomass”. *Energy Conversion and Management*. 2000. 41 (6), 633-646.

[25] Mamleev V, Bourbigot S, Yvon J. “Kinetic analysis of the thermal decomposition of cellulose: The change of the rate limitation”. *Journal of Analytical and Applied Pyrolysis*. 2007. 80 (1), 141-150.

[26] Varhegyi G, Jakab E, Antal MJ. “Is the Broido-Shafizadeh Model for Cellulose Pyrolysis True?” *Energy & Fuels*. 1994. 8, 1345-1352.

[27] Wershaw RL. “Evaluation of conceptual models of natural organic matter (humus) from a consideration of the chemical and biochemical processes of humification”. *Reston, Va.: U.S. Dept. of the Interior, U.S. Geological Survey*; Denver, CO : U.S. Geological Survey, Information Services [distributor], 2004.

Concluding Remarks

Following the eighth quarterly report, work continued on including oxygen chemistry in INGen (the Interactive Network Generator). It was necessary to establish the complete list of relevant reaction types in order to generate an accurate biomass pyrolysis kinetic model. Reaction site neighborhoods and reactivity rules were identified for new pathways-level reaction types including keto-enol tautomerization, aldehyde hydrogenation, ketone hydrogenation, and alcohol dehydration, among others. Forthcoming molecular-level composition data will allow for kinetic parameter tuning in KME (the Kinetic Modeling Editor). Using the accurately tuned kinetic parameters for the new reaction types in the cellulose pyrolysis network will result in a more comprehensive biomass pyrolysis model.

Attachments

The source code for four models have been included along with this report. The files were compiled under the Cygwin environment with the gcc compiler. In addition, the raw results of simulation were included as an attached Excel file.